Ice water content assessment in the single-, dual-, and triple-frequency radar scenarios

Eugenio Gorgucci, Luca Baldini, Elisa Adirosi, and Mario Montopoli

Istituto di Scienze dell'Atmosfera e del Clima (CNR)
Area della Ricerca Roma-Tor Vergata
Via Fosso del Cavaliere, 100 - 00133 Rome, Italy

Corresponding author: e.gorgucci@isac.cnr.it

Original manuscript submitted to

Remote Sensing of Environment

08/10/2020

Abstract

With the advent of the Global Precipitation Measurement (GPM) mission and the associated Ground Validation campaigns, there has been a strong development of studies related to dual-frequency and more recently to triple-frequency radar. In this context, one requirement is that at least one of the radar frequencies operates in the Rayleigh regime while the others have to ensure a measurable difference in reflectivities. A common radar coupling for triple frequency systems is the Ku-, Ka-, and W-band.

Multi-frequency radars, in addition to the classic single-frequency reflectivity (SFR) measurement for each frequency, allow a further parameter, the dual-frequency ratio (DFR) defined as the ratio between two reflectivities at two frequencies. Referring to the same measurement volume, and for a fixed microphysical ice particle model, SFR and DFR allow to better constraint parameters of the particle size distribution, such as the mass-weighted mean diameter (D_m) and the normalized intercept parameter (N_w) when a normalized gamma distribution is assumed.

This paper deals with various topics with the preliminary purpose of assessing the accuracy of the ice water content (IWC) estimate obtained using SFR and DFR methods to evaluate the improvements brought by the use of DFR. To pursue this goal, a simple microphysical model was used to choose the form of the SFR and DFR estimation algorithms and to evaluate their performances in a simulated framework.

The most important aspect revealed by the study is that the cloud water content (CWC) plays a very important role both in the mass vs. diameter relationship as well as in the IWC estimation. The combined use of specific radar algorithms according to the different CWC values has shown notable improvements for the IWC estimation. Since CWC is not an operational measure, a substitute parameter was sought in the (DFR_{aou}, DFR_{woa}) domain defined by the Ka- and Ku-band and by the W- and Ka-band measurements. This new parameter provides improvements similar to those obtained with the use of CWC.

Data from the OLYMPEX field campaign that include an airborne triple-frequency radar at Ku-, Ka-, and W-band, as well as airborne measurements of in-situ bulk microphysics and meteorological parameters were used to validate the robustness of the methodology.

1. Introduction

Upper-tropospheric ice clouds play an important role in affecting the global radiation budget and climate system, as shown by satellite observations and general circulation models. Ice microphysical processes are an important part of cloud and precipitation formation and then of the water cycle since most surface precipitation begins as ice particles (Field and Heymsfield, 2015). In light of these considerations, the importance of accurately estimating ice water content (IWC), which is a central parameter for cloud microphysical studies and for understanding the effects of clouds on the global radiation budget and climate system (Stephens, 2005), appears evident.

IWC is defined as the ice mass per unit volume of atmospheric air and it is generally estimated as the particle's mass weighted integral of measured particle size distributions (*PSD*s). An ice crystal model expressing the crystal mass as a function of the particle's diameter is usually assumed, in which the particle's diameter is the diameter of an equivalent sphere that describes the volume occupied by air and ice.

In the last decade, several measurement campaigns aimed at characterizing the global atmospheric ice mass were carried out in different climatological regions. In these campaigns [i.e. MC3E (Jensen et al., 2016), GCPEX (Skofronick-Jackson et al., 2015), IPHEx (Barros et al., 2014), OLYMPEX (Houze et al. 2017)], aircrafts were used as platforms for remote sensing instruments and for in-situ measurements of the microphysical, thermodynamic, and kinematic properties of ice crystals. In this way, the characterization of the number and size of ice particles within clouds can be performed both directly with in-situ aircraft probe observations and indirectly with active remote-sensing instrumentation. Near-coincident and near-simultaneous recordings of radar observations in conjunction with in-situ probes sampling of ice crystals form an ideal framework for testing combined retrieval techniques that make use of cloud radar observations.

Due to their short wavelengths, cloud radars can be quite sensitive to ice crystals and can be designed to have high temporal and spatial resolutions operating with antennas that have narrow beam widths while maintaining a reasonable size. For this reason, especially for airborne and spaceborne platforms, millimeter-wave radar has emerged as an important tool in the identification and characterization of cloud ice crystals as well as their quantification in terms of IWC and snowfall rate estimations.

The strong variability in the shape, density, and size of ice crystals contributed to investigating an approach that makes use of dual-frequency radars, which in principle offer one more measurement in the same visited resolution volume than in the single-frequency reflectivity (*SFR*) approach (Matrosov et al. 2005). For the dual-frequency ratio (DFR) approach, the choice of the two frequencies is made in such a way that for one, scattering is in the Rayleigh regime in terms of the monotonic increase of backscatter efficiency with particle size while for the other it is in the Mie regime. In this context, it is possible to define the DFR as the ratio of the equivalent radar reflectivity factors at two different selected frequencies (Matrosov et al., 2005; Liao et al. 2016). This new parameter can be used in rain to estimate D_m, which is defined as the ratio of 4th moment to 3rd moment of the PSD expressed in terms of the liquid equivalent median mass diameter (Liao et al. 2016).

The DFR technique represents an important step forward in realistically assessing ice cloud parameterization and has greater potential for estimating IWC. Nevertheless, the limit determined by the fact that the equivalent reflectivity factor depends on the backscattering cross-section of the ensemble of the particles inside the resolution volume, and only indirectly on their mass through the particle's dielectric constant, remains unavoidable. Consequently, any IWC estimates based on radar reflectivity factors will show high uncertainty, thus making it difficult to choose a single ice model to represent the actual population of ice particles.

The problem would be relieved, as is the case for raindrops, if there were an appropriate particle habit that well represents the majority of the ice particle population. Unfortunately, in-situ observations of ice cloud particles have consistently shown both their complex geometry and the presence of different habits in the same sampling volume. The size of ice cloud particles ranges from microns to centimeters and their habits vary from simple pristine ice crystals to extremely irregular aggregates (Heymsfield et al., 2002; Heymsfield, 2003). This variability, due to changing growth regimes in different temperature conditions, generates significantly different microwave scattering properties, and no reliable method yet exists to directly estimate ice habits from microwave remote sensing.

To quantify scattering properties, assumptions about ice habits must be made that can result in large uncertainties in derived estimates of IWC. Consequently, in recent years many studies have been devoted to investigating the scattering properties of ice crystal shapes using more realistic modelling. In some cases, this has allowed the creation of databases providing scattering parameters such as backscatter cross-section and extinction coefficient as a function of particle size for various ice types (Tyynelä et al., 2011; Leinonen et al., 2012; Hogan and Westbrook, 2014; Ori et al., 2014; Leinonen and Szyrmer, 2015; Kuo et al., 2016).

Both scattering simulations using soft spheroid particle models and databases for different ice habits have shown that the combination of Ku-, Ka-, and W-band frequencies could be of particular relevance for discriminating between different ice habits (Petty and Huang, 2010; Kneifel et al., 2011; Leinonen et al., 2012; Kulie et al., 2014; Tyynelä and Chandrasekar, 2014; Leinonen and Moisseev, 2015; Leinonen and Szyrmer, 2015). The domain defined by the DFRs between Ka- and Ku-reflectivity (DFR_{aou}) versus the DFRs between W- and Ka-reflectivity (DFR_{woa}) revealed a separation between the aggregate and the spheroid particle models. Therefore, thanks to the ability of classifying various ice types, the combined use of the triple-frequency radar reflectivity signatures is expected to provide more accurate quantitative estimations of ice water content. However, it is worth noting that DFR_{aou} vs. DFR_{woa} trend for dendrites and needle aggregates has shown a highly non-monotonic behavior, leading to have two values of DFR_{aou} for a fixed DFR_{woa} (Petty and Huang, 2010).

This study is aimed at developing IWC algorithms based on DFR methods and evaluating their accuracy compared to SFR algorithms. A very important result of the study is to highlight the benefit that the knowledge of cloud water content (CWC) has both in determining the mass-size relationship and in estimating IWC. The combination of several estimation algorithms, each of them tuned according to some CWC intervals, shows a better performance than using a single algorithm. As CWC is usually unavailable in operational contexts, a replacement parameter in the DFR domain was identified, making the proposed methodology independent of the availability of ancillary information. Data from the OLYMPEX field campaign that include an airborne triple-frequency radar at Ku-, Ka-, and W-band, as well as airborne measurements of in-situ bulk microphysics and meteorological parameters, were used to validate the results.

The paper is organized as follows: Section 2 describes the equations governing the scattering properties and the bulk cloud microphysics of ice particles. Section 3 gives an overview of the field measurement campaign from which the in-situ data were extracted for algorithm validation. Section 4 provides a summary of the most common empirical mass-size relationships for deriving IWC and the relative results obtained by applying them to the field measurements. Section 5 shows algorithms found relating IWC measurements to the coincidental PSD measurements from the field campaign without assuming any predetermined relation. Section 6 describes IWC algorithms based on the reflectivity measurements and in combination with the DFR*s*. Section 7 evaluates the behavior of algorithms using both simulated and experimental measurements of collocated triple-frequency radar observations and in-situ microphysical measurements of IWC. Section 8 describes a new way of looking at the DFR domain and, more precisely, how use it to obtain improved estimates of bulk parameter such as the IWC. Finally, the summary and conclusions are drawn in Section 9.

2. Bulk cloud microphysics and scattering properties of ice particles

Basically, a single-frequency weather radar observes any liquid or solid hydrometeor through the backscattered power it receives after transmitting electromagnetic radiation in the atmosphere. The received power $P(r)$, which is a function of the distance between the radar and the ensemble of hydrometeors (r), is proportional to the measured radar reflectivity factor $\xi_m(r)$ through

$$P(r) = \frac{C}{r^2} L \xi_m(r) \qquad (1)$$

where C is the radar constant characterized by the radar system properties and L is the loss factor that take into account the attenuation of signal propagating through a medium filled by hydrometeors. An equivalent radar reflectivity factor $\xi_e(r)$ is defined as:

$$\xi_e(r) = \frac{\lambda^4}{|K_w|^2 \pi^5} \int_0^\infty N(D)\sigma(D)\,dD \qquad (mm^6\,m^{-3}) \qquad (2)$$

where $N(D)$ is the particle size distribution (PSD), $\sigma(D)$ is the backscattering radar cross-section of particles with diameter D, K_w is the complex dielectric factor of water, and λ is the radar wavelength. One key element in (2) is the *PSD*, which is defined as the number of particles per unit volume per unit size interval (D to $D+\Delta D$). A gamma distribution model has been successfully used to adequately describe many of the natural variations in rain of the particle size distribution (Ulbrich 1983). In nature, $N(D)$ is characterized by a wide variability. To avoid a statistical dependence of the gamma distribution parameters, Testud et al. (2001) proposed scaling the raindrop size D and $N(D)$ in such a way that *PSD*s are independent of the mass-weighted mean diameter (D_m) relation and liquid water content (LWC). Delanoë et al. (2005) extended this concept to ice particle size distribution. Therefore, a normalized gamma function is described in terms of three physical quantities: the normalized intercept (N_w), which is a function of the LWC; the mass-weighted mean diameter (D_m); and the shape factor μ. The relation is represented by the equation

$$N(D) = N_w f(\mu) \left(\frac{D}{D_m} \right)^{\mu} \exp(-\Lambda D) \qquad (mm^{-1}\,m^{-3}) \qquad (3)$$

where

$$f(\mu)=\frac{6}{(3.67)^4}\frac{(3.67+\mu)^{\mu+4}}{\Gamma(\mu+4)}, \tag{4}$$

$$\Lambda=\frac{\mu+4}{D_m} \quad (mm^{-1}) \tag{5}$$

and D_m for liquid is the ratio between of the fourth to the third moment of the PSD

$$D_m=\frac{\int_0^\infty N(D)\,D^4\,dD}{\int_0^\infty N(D)\,D^3\,dD} \qquad (mm) \tag{6}$$

and

$$N_w=\frac{4^4}{\pi\rho_w}\left(\frac{LWC}{D_m^4}\right) \qquad (mm^{-1}\,m^{-3})\,. \tag{7}$$

where ρ_w is the density of water and LWC is proportional to the third moment of the PSD as follows

$$LWC=\frac{\pi\rho_w}{6}\int_0^\infty N(D)\,D^3\,dD \qquad (g\,m^{-3}) \tag{8}$$

Therefore, the statistical distribution of the cloud particle size in the radar-sampled volume is characterized by the two parameters N_w and D_m if μ is obtained through some assumptions. Williams et al. (2014) showed that for rain μ is not totally independent by N_w and D_m, and it can be related to them through an empirical relationship. More recently, Borque et al. (2019) found a similar relationship for ice crystals. Hence, using a statistically μ-D_m relationship for ice phase, the unknown parameters characterizing the PSD can be reduced to two and therefore they can be found solving a system of two independent equations. Moreover, atmospheric attenuation from hydrometeors, cloud water, and water vapor generally increases with radar frequency. However, analysis on different ice types show that attenuation is quite small at the Ku- and Ka-bands but can be significant at W-band. Thus, ξ_e in general must take the attenuation into account:

$$\xi_e=A(r)\,\xi_m \tag{9}$$

where $A(r)$ is the two-way path attenuation of the wave at distance r.

IWC is a central parameter for cloud microphysical studies for its fundamental implications with regard to the effects on the global radiation budget and climate system. IWC is defined as the cloud mass of ice per unit volume of atmospheric air

$$IWC = \int_0^\infty m(D)N(D)\,dD \qquad (g\,m^{-3}) \tag{10}$$

where $m(D)$ is the mass of ice crystals having diameter D. In light of what has been argued above, equation (10) can be represented as a function of at least three variables, N_w, D_m, and ρ_e, which is the density of the mixture (or effective density) of the ice particle. Therefore, to describe ice cloud integral properties one needs to know at least three parameters or know relations among some of these parameters to decrease the degree of freedom. Unfortunately, no reliable relationship between ice crystals' size and particle density is known.

An appropriate formulation of hydrometeor microphysics is a prerequisite for modeling radiative properties. In recent years, a suitable formulation to approximate more realistic ice crystals when computing their microwave-scattering properties was proposed in the Discrete Dipole Approximation (DDA) (Liu 2008; Kulie et al., 2010; Tyynelä et al., 2011; Botta et al., 2011; Leinonen et al., 2012). From a practical point of view, within the same cloud, the structure of each single ice crystal is random and unpredictable, as well as the ice crystals' habits, which occur in a virtually limitless variety of geometries. This behavior arises from the fact that an ice crystal is affected by different environmental conditions as it travels through the cloud, leading to the conclusion that it seems unrealistic to assume that only a single crystal shape is present within a cloud. It follows that the scattering properties of a radar measurement volume containing an ice crystal ensemble will be the result of individual backscattering from different ice shapes. Unfortunately, there is no single parameter that can give comprehensive information about the particles' microphysical properties.

An alternative approach is the soft sphere approximation, i.e. those particles that thanks to their irregular low density, are optically “soft”, namely their equivalent refractive indices are close to 1, that provides a means to compute the scattering properties of a single ice particle having the shape of a sphere or a spheroid. This simplified method is computationally very efficient. In this approach, the soft particle is assumed to consist of a homogeneous ice and air mixture where its effective density ρ_e, is less than the density of pure ice (Matrosov, 1998). It is worth noting that while the soft spheroid assumption is acceptable for Ku-band and possibly even for Ka-band, it is not always appropriate for W-band because can lead to a crude approximation.

With the advent of the GPM era, these retrieval methods have been applied to dual-frequency space-borne radars that made possible to infer the microphysical and radiative properties of ice clouds (Ni et al. 2019), avoiding the uncertainty related to effect on the radar signal due to the melting layer experienced by ground-based observations. The use of two radar frequencies is appealing because it allows defining a dual Dual Frequency Ratio (DFR) as the ratio between the two reflectivity factors ξ_1 and ξ_2, where 2 and 1 represent the lowest and the highest frequency, respectively,

$$DFR = \frac{\xi_{e1}}{\xi_{e2}} = \frac{(\lambda_1)^4 \int_0^\infty N(D) \cdot \sigma_1(D) dD}{(\lambda_2)^4 \int_0^\infty N(D) \cdot \sigma_2(D) dD} \tag{11}$$

that shows a predictable relation with D_m and has the advantage of being quite immune to variations of particle density ρ_e, N_w, and μ. Consequently, the use of DFR can give independent estimates of hydrometeor effective size with a greater precision with respect to more established radar methods (Matrosov 1998; Liao et al., 2016).

From (2) and (3), it would seem that DFR is independent of N_w and, once μ is fixed, it is a function of D_m alone. However, in practice, equation (11) is the result of different effects due to the polydisperse ensemble of ice particle habits and masses, and therefore the quantity D_m can be considered a statistical parameter (Sy et al., 2020).

In recent years, modeling studies based on monodisperse hydrometeor habits have observed that, since backscattering cross-sections are a function of frequency, by combining DFRs computed using different pairs of frequencies, it may be possible to define a domain in which the different hydrometeor classes occupy distinct regions (Liu 2008; Kneifel et al., 2011). More specifically, such domain is usually defined by the DFR computed using Ka and Ku bands and the DFR computed using W and Ka band, represented along the ordinate and abscissa, respectively. More recently, although in qualitative form, verification studies have been conducted using airborne radar observations with coincident airborne microphysical measurements that have confirmed the theoretical results obtained from the simulation models (Kulie et al., 2014; Chase et al., 2018).

3. The OLYMPEX field measurement campaign

In order to pursue the goals of this study, an extensive use was made of the data collected during the Olympic Mountains Experiment (OLYMPEX). This measurement campaign, part of the Global Precipitation Measurement (GPM) Mission Ground Validation program, took place between November, 2015, and January, 2016, and was focused on the characterization of mid-latitude frontal rain and snow over the complex terrain of the Olympic Peninsula region of Washington State (Houze et al. 2017).

During OLYMPEX, two aircrafts were used: the University of North Dakota (UND) Citation and the National Aeronautics and Space Administration (NASA) DC-8. The UND Citation was equipped with state-of-the-art instrumentation to give the best possible representation of the cloud microphysical conditions. The instruments include, among others, the NCAR Particle Probes (NPP), providing in-situ PSDs over the size range from about 50 μm to 3 cm; the Nevzorov (NEV) probe, providing both the total water content (TWC) and the liquid water content (LWC); the King Probe giving a further measure of the liquid water content (KLWC); the Rosemount ice detector (RID) and the Cloud Droplet Probe (CDP), giving the cloud liquid water content (CWC) by measuring the concentration and size distribution of cloud droplets in the size range from 2-50 µm.

Actually, NPP combines spectra obtained from two optical array probes: the array of a 2-Dimensional Stereo (2DS) probe (Lawson et al., 2006) and the High Volume Precipitation Spectrometer Version 3 (HVPS3) probe (Heymsfield et al., 2015; Giangrande et al., 2016) both equipped with antishattering tips and processed using the technique described in Field et al. (2006). The Nevzorov probe (Korolev et al., 1998) is a constant-temperature hot-wire probe and consists of two separate sensors, one for measuring LWC and the other for TWC. The King probe is an additional wire-based probe that alters its resistance as the encountered liquid water evaporates whose variation provides the KLWC. The RID is an oscillation probe whose operating principle is determined by the decrease of the vibration frequency caused by the ice accumulation above the tip of the sensor providing atmospheric icing rates and cloud liquid water contents. The CDP is a forward-scattering optical spectrometer in which cloud droplets passing through a focused beam of a diode laser can be detected allowing to evaluate the effective droplet radius, the total droplet number concentration and the cloud water content.

The DC-8 carried the Airborne Precipitation Radar Third Generation (APR3). APR3 is a triple-frequency radar operating at Ku-, Ka-, and W-band obtained as an enhanced version of the APR2 radar (Sadowy et al., 2003) with the addition of the W-band channel. The radar looks downward and scans its antenna across track from 25° to the left and right of nadir once every 2 seconds and with the range gates 30 m apart (Tanelli et al., 2006).

Validation of the reflectivity calibration was performed against the ocean surface return (Tanelli et al., 2006). Moreover, in the highest part of the cloud, where there are usually very small ice particles for which it is possible to hypothesize a Rayleigh scattering for all the three radar frequencies, the reflectivities were compared with each other and showing a spread of about 1 dB. Furthermore, with these reflectivity measurements, the distribution as a function of the bin position was found for determining the minimum detectable signal at each frequency and verified the absence of bias in the multifrequency radar observations, i.e. the power ratios between the bands Ku/Ka, Ka/W, and Ku/W.

During the OLYMPEX campaign, the DC-8 aircraft flew above the clouds at mostly constant altitude (10 km) while the Citation flew at lower altitudes, performing constant altitude flights through the clouds. The flight plans ensured that the APR3 intersected the Citation to allow near-coincident measurements of radar and microphysical data.

In this study, for a more accurate and in-depth investigation of cloud ice microphysical conditions the combined measurements of the NPP, the Nevzorov, the King probes, the RID and CDP are used to evaluate the contribution of the triple-frequency radar to the knowledge of the bulk cloud properties with particular attention to the ice water content estimation.

4. Ice water content and particle size distribution

Equation (10) shows that the IWC can be derived from the distribution of ice particle sizes once the mass-size distribution within each particle size is known. In practice, depending on the instrumentation used, the hydrometeors are detectable within finite size intervals ranging from a minimum (D_{min}) to a maximum diameter (D_{max}). Then, (10) is practically obtained as a sum as

$$IWC = \sum_{D_{\min}}^{D_{\max}} N(D)\, m(D)\, \Delta D \,. \qquad (12)$$

Due to the irregular shape of ice crystals, the definition of D, for which no standard convention exists, plays a critical role as it can change the bulk cloud properties when they are determined from observed PSDs. In this study, D is considered to be the diameter of the sphere that entirely contains the ice particle. This implies that, from a practical point of view, D is not directly related to the particle's mass m and, consequently, it is necessary to use empirical m-D relations.

In-situ measurements have indicated that the density of snowflakes commonly decreases with their size. The empirical expressions most frequently used to predict the mass for various types of ice crystal shapes are expressed through a power law (Heymsfield et al., 2004; McFarquhar et al., 2007; Brandes et al., 2007) as

$$m = \frac{\pi}{6}\rho_e D^3 = aD^b \quad (g) \tag{13}$$

where m is again in grams, D is in centimeters, ρ_e is the particle effective density, a is the pre-factor coefficient (in cgs units), and b is the exponent of the power law. The ice hydrometeor mass usually increases with size more slowly than its volume, thus requiring the density ρ_e to be inversely proportional to the diameter D and therefore, the exponent b generally is less than 3. The coefficients in (13) on average depend on the ice crystal habits, temperatures, and particle sizes that are present in the cloud, contributing to a wide set of different mass-diameter relationships. Specific relations for each distinct habit could not find an effective application in the retrieval of the mass because, in a cloud, the habits of the ice crystals are not known a priori and, in reality, they are of mixed and complex types as they arise from the multiple meteorological conditions that exist in clouds.

For a general characterization of the in-situ measurements collected from the Citation aircraft during the OLYMPEX campaign, an appropriate way is to start by observing to what extent the classical m-D relationships are able to describe the bulk property behavior. For this purpose, it was convenient to choose a set of m-D relationships that are general enough to encompass the widest spectrum of weather conditions. Because of its ability to represent a wide range of habits such as aggregates of unrimed bullets, columns, side planes, and quasi-spherical particles, the extensively used Brown and Francis (1995) relationship (hereafter BF95) was selected. In addition, the two parametrizations put forth by Heymsfield et al. (2004) were used because of their capability to describe the variability of the conditions encountered by ice crystals in convective and stratiform storms. The first of the two relations (hereafter H04syn) was found from synoptic systems that are typically responsible for winter snowfall, whereas the second one (hereafter H04cnv) was originated from convective clouds. A further algorithm by Heymsfield et al. (2010) was used in this analysis (hereafter H10all). The H10all algorithm was found by imposing the condition that it had the best performance regardless of values of the IWC and temperature present in the cloud. It was developed using a large dataset of PSD and IWC aircraft observations, obtained by merging six datasets collected during distinct campaigns conducted under different weather conditions.

Eventually, the additional relationship for the unrimed or lightly rimed aggregate snowflakes obtained by Szyrmer and Zawadzki (2010) (hereafter SZ10ave) was used in this paper. In this case, the coefficients of (13) were found by averaging the coefficients *a* and *b* of nine snowflake events regardless of the ground temperature. The nine relationships were derived from a dataset of low-density snow aggregate measurements collected by a ground-based optical disdrometer. Table I summarizes the coefficients *a* (in cgs units) and *b* of (13) corresponding to the selected *m-D* relations described above. Each entry in Table I represents a pair of parameters in (13) that we indicated with the vector $\mathbf{p}_{LI}$, where "**p**" and subscript "*LI*" stand for parameters and from the literature, respectively. As a result, when we put (13) into (12) we have an IWC(PSD, $\mathbf{p}_{LI}$) estimate that depends on a PSD and coefficients $\mathbf{p}_{LI}$. In general, the notation IWC(x, $\mathbf{p}_y$) indicates the IWC estimate obtained using input data identified by the string *x* and the vector of coefficients $\mathbf{p}_y$.

The main problem to validate any ice microphysics parameterization is to verify the performance of its outputs with respect to the real environmental measurements keeping in mind that each measuring instrument has its limitations and sources of error. Unfortunately, this one still remains a long-standing experimental problem exacerbated by the fact that ice is mostly present in mixed-phase and the separation of ice from water presents technical difficulties.

Cloud IWC from airborne measurement is derived directly by bulk microphysical probes and during the OLYMPEX campaign, the Citation aircraft was provided with state-of-the-art instrumentation for making the most reliable cloud microphysical measurements.

The cloud spectrometer and impactor (CSI) provides a good measure of IWC after separating cloud droplets and ice crystals from interstitial water vapor (Twohy et al., 1997). Unfortunately, it could not be used because during the campaign it was not trustworthy.

In the context of the Olympic measurement campaign it was evaluated that the most suitable and trustworthy aircraft instruments to characterize the cloudy environmental physical conditions were the King probe for the liquid water content (KLWC) and the Nevzorov probe for the total water content (TWC). Therefore, in cloud regions with temperatures below the freezing point, the positive values of the differences

$$EIWC = TWC\,(Nevzorov) - KLWC\,(King) \tag{14}$$

were taken as measure of the environmental Equivalent Ice Water Content (EIWC). In this way, it was possible to overcome the lack of the IWC measure provided by the counterflow virtual impactor (CVI) that was not functioning properly during the OLYMPEX field campaign. It should be emphasized that EIWC will be affected by an error that depends on the errors of the King and Nevzorov probes that have unknown magnitudes as they depend on the environmental conditions encountered. In particular, these two errors are of opposite sign: in fact, the first is determined by an overestimation of the LWC provided by the King resulting from the interaction of ice crystals with hot wire (Cober et al., 2001), while the second results in an underestimate of the Nevzorov IWC by a non-negligible amount when ice particles are relatively large D>4 mm (Korolev et al. 2013). In fact, even with the deep dish probe, they can bounce out of the collection cone or can hit the edge of the inlet and fragment, with the fragments not entering the inlet where they are sensed. This situation is such that underestimation is minimal at the lower IWCs and increases as the IWC increases reaching factors greater than 2 (Abel et al. 2014). Within the above mentioned caveat, considering the OLYMPEX dataset, we compared the calculation of IWC(PSD, $\mathbf{p}_{LI}$) using (12) with measurements of (14). For this comparison, only those samples collected at temperatures below 0 °C were selected which, as shown in Figure 1, represent the condition under which the vast majority of airplane measurements were carried out. Besides, we considered only those PSDs that registered at least one count for three size bins larger than 137.5 microns (fifth bin) that is the bin closest to 150 microns (Kingsmill et al. 2004). Following this selection procedure, we found a total of 100220 of 1-s PSDs with a valid measure of EIWC.

Table II depicts the error performance of the various m-D parameterizations of Table I with respect to the reference EIWC. To quantify the performance of each algorithm the following merit factors are considered: the normalized standard error (NSE) defined as the root mean square error normalized to the true mean value of the entire dataset, the normalized bias (NB) as the mean difference normalized to the true mean value, for which a negative value means an overestimation of the estimated value, and the Pearson correlation coefficient (ρ) as the measure of the strength of a linear relationship between the two variables being compared.

The analysis shows a good behavior of ρ for all the algorithms ranging between the lower 0.7582 of the H04cnv and the upper 0.8793 of the SZ10ave whereas NSE and the NB exhibit poor behavior for all the algorithms, with BF95 having the lowest values of NSE and NB equal to 1.36 and -0.87, respectively. Figure 2 shows the 2-D histogram between the direct EIWC measurements versus the corresponding estimate IWC(PSD,BF95) for the entire dataset.

These comparisons are mainly affected by the assumptions made regarding the ice crystal density and its habit, which are, among other things, influenced by temperature and by riming. Riming is a process involving the collection of supercooled water droplets of few microns in diameter onto the ice surface. To get insights on the performance of the different algorithms with respect to the meteorological conditions, in situ ancillary measurements of temperature and CWC were taken into consideration.

For each frequency group, *a* and *b* parameters in the m-D relation were found by minimizing the difference between the IWC obtained by (12) and the measured EIWC. By comparing the various *a* and *b* parameters obtained (not shown), we verified a substantial similarity among them with small differences among the respective merit factors. From this result, we deduced that the IWC measurements alone do not allow discriminating against the different ice conditions.

The CDP provides a quantitative measurement of the liquid content and therefore it can facilitate a more precise partitioning. In this perspective, to evaluate the effect of riming on ice mass relations, the CDP was used as an independent measure of the CWC produced widely by the small supercooled drops (2-50 μm) that are present in very large numbers in mixed-phase clouds. These measurements are generally affected by underestimation due to non-sampling of the largest drops and by a bias that is strongly concentration-dependent, both of unknown magnitudes.

Taking into account the distribution of the CWC measurements, an arbitrary subdivision was made into six class according the intervals: *i*) CWC$\leq 10^{-5}$ g/m^{-3}, *ii*) $10^{-5}<$CWC$\leq 10^{-3}$ g/m^{-3}, *iii*) $10^{-3}<$CWC$\leq 10^{-2}$ g/m^{-3}, *iv*) $10^{-2}<$CWC$\leq 10^{-1}$ g/m^{-3}, *v*) $10^{-1}<$CWC≤ 1 g/m^{-3}, *vi*) CWC>1 g/m^{-3}. The behavior of the mean difference between the in-situ measurements of EIWC with the respective estimates obtained by each $\mathbf{p}_{LI}$ as a function of the cloud temperature and the CWC were analyzed. Figure 3a shows the trend of the mean differences between EIWC measurements and IWC(PSD, $\mathbf{p}_{LI}$) as a function of temperature. It is evident that for temperatures lower than -30 °C the performance of each algorithm is quite good and has almost negligible bias, with H04cnv presenting the best behavior. As the temperature increases, each algorithm has an increasing negative mean difference indicating an overestimation with respect to the corresponding in situ measurements. In this context H10all and BF95 have the least variation with temperature and the latter shows the best performance. Figure 3b summarizes the analysis of the behavior of the five algorithms in the presence of cloud water described in terms of CWC. Moving from almost dry environments (10^{-5} g/m^3) to increasing degrees of water content, the algorithms reveal different behaviors with the common tendency to overestimate EIWC, similarly to the increase in temperature of Fig. 3a. In addition, in this case BF95 performs better, presenting the lower overestimation. Furthermore, it should be stressed that for CWC>0.1 g/m^3 the algorithms show a strong overestimation with the only exception for H04cnv. This overestimation could be because of the known Nevzorov probes deficiencies (Korolev et al. 2013; Abel et al. 2014).

5. Tuned IWC algorithm for the OLYMPEX dataset

For a more specific comparison between the IWC estimates and the EIWC measurements, it is convenient to tune the parameters of (13) by minimizing the differences between $\mathrm{IWC}(\mathrm{PSD}, \hat{\mathbf{p}}_{pp})$ and EIWC, where the subscript *pp* indicates that parameters are obtained using experimental data from a particle probe. The estimated coefficients $\hat{\mathbf{p}}_{pp}$ were obtained by considering coincident observations at all temperatures below 0 °C.

For the OLYMPEX experimental dataset, the coefficients $\hat{\mathbf{p}}_{pp}$ are a=1.92×10^{-3} and b=2.044, while the performance of $\mathrm{IWC}(\mathrm{PSD}, \hat{\mathbf{p}}_{pp})$ in terms of the merit factors is characterized by NSE=0.53, NB=0.13 and ρ=0.8735.

Following the procedure used above, the *a* and *b* parameters were found for each of the considered CWC intervals, allowing computing $\mathrm{IWC}(\mathrm{PSD}^{ci}, \hat{\mathbf{p}}_{pp}^{ci})$ where *ci* identifies one of the CWC class intervals defined above. Table III shows the parameters for the different CWC classes, while Fig. 4a shows the exponent *b* as a function of the prefactor *a* (black star-ring) highlighting an evident relationship between the two parameters. This relationship can be expressed by interpolating the experimental parameters with a third-degree polynomial function as

$$b = 5.239 \cdot 10^{8} a^{3} - 2.956 \cdot 10^{6} a^{2} + 6030 a - 2.24. \qquad (15)$$

On average, Fig. 4a depicts the influence of riming process on the m-D relation for the entire period when the OLYMPEX campaign took place. Although the relation shows a monotonically increasing behavior, three different trends can be observed. In the first stage (prefactor a<1.6 10^{-3}), the exponent *b* has a decreasing growth rate to reach an inflection (second stage with 1.6 10^{-3}<a<2 10^{-3}), to reach a faster growth rate for larger a (third stage with a>2 10^{-3}). Fig. 4b displays the prefactor *a* versus the CWC mean value of the corresponding group from which the existence of a relation between the CWC and the prefactor *a*, and consequently, also with the exponent *b* through (15), can be inferred. Such *a* vs. CWC mean value can be expressed by means of a third-degree polynomial as

$$CWC = 4.981 \cdot 10^{8} a^{3} - 1.969 \cdot 10^{6} a^{2} + 2696 a - 1.26. \qquad (16)$$

From the joint analysis of Figs. 4, it is possible to infer that the different stages of the mass-size relationship correspond to different riming conditions, for which the first stage corresponds to a substantial dry environment (hereafter dry regime), followed by a second stage where CWC slowly begins to grow (hereafter moist regime) (Leinonen and Szyrmer, 2015), and by a third one with a rapid growth trend (hereafter wet regime). This tendency is partially in agreement with Tridon et al. (2019) and the three stages can be interpreted as follows. During the dry stage, ice crystals are allowed to clump together to form snowflakes changing their mass-size relation. Throughout the second stage the efficiency of dry growth decreases and, at the same time, with the beginning of the presence of water, the riming process described by the fill-in process (Heymsfield 1982) takes place. Both ice density and air temperature modulate this growth between filling internal crystal interstices or supporting external growth. At the end, although it is not shown in Figs. 4, when the empty spaces inside the ice particles are full, the collection of the water from the environment is used entirely for modifying their shapes.

Applying $\mathrm{IWC}(\mathrm{PSD}^{ci}, \hat{\mathbf{p}}_{pp}^{ci})$ with the parameters reported in Table III for the corresponding CWC intervals, the performance of (12) was assessed in terms of the merit factors. Fig. 5a depicts NSE, NB absolute value, and correlation coefficient as a function of the CWC interval. NSE has quite similar values in the first four intervals, i.e. for CWC≤0.1 g/m^3, with an average value of 0.47. For larger CWC, it has a jump that brings it to about 0.64 in the two wettest intervals. The absolute value of NB shows a trend fluctuating between 0.01 and 0.1. As far as ρ is concerned, it has a value of 0.845 in the first interval and takes increasing values up to the *iv* interval where it reaches the value of 0.888. Then, it decreases sharply until reaching 0.23 in the last interval indicating an increasing decorrelation between estimates obtained by (12) and measurements for CWC>0.1 g/m^3.

In practice, CWC is not usually known, and hence it would be necessary to use the general relation $\mathrm{IWC}(\mathrm{PSD}, \hat{\mathbf{p}}_{pp})$ instead of the CWC tuned ones. $\mathrm{IWC}(\mathrm{PSD}, \hat{\mathbf{p}}_{pp})$ presents different performances depending on CWC group as shown in Fig. 5b. The merit factor behaviors are modulated by the distribution of the mean square errors of $\hat{\mathbf{p}}_{pp}$ with respect to the corresponding measurements in the different CWC groups. In general, except for ρ, which has a behavior similar to that shown by the $\mathrm{IWC}(\mathrm{PSD}^{ci}, \hat{\mathbf{p}}_{pp}^{ci})$, NSE and NB show larger values. Both exhibit a decreasing trend until reaching a minimum for CWC≤0.1 g/m^3 and then NSE grows again for larger CWC while NB remains small and constant. In the fourth group where they reach the minimum, the values of the merit factors are comparable to those obtained using the corresponding class-specific parameterization.

6. IWC retrieved from radar measurements

Remote sensing methods have been used extensively to investigate ice cloud microphysical characteristics and, in the course of the past few years, have achieved further improvements by the millimeter-wave radars on board satellites. The most widely used radar variable for retrieving the cloud bulk parameters is the equivalent reflectivity factor that is connected to the ice particle size distribution and to the shape of each individual ice particle from which the resulting scattering properties are derived.

Unfortunately, in the context of the radar frequencies used for ice particle studies, from channels above the Ku-band, there is less possibility of considering as true the condition that the particle size is much smaller compared with the incident wavelength, which is of primary concern for the application of Rayleigh scattering theory. Consequently, we cannot handle in an easy analytical way the radiative interactions between the incident power and the ice particles. This is even more true considering the impossibility of exactly knowing a parameter characterizing the ice particle size distribution such as D_m, or being informed of individual particles' habits or of defining a habit able to represent all particles as well as by the lack of knowledge of the mass distribution inside every single crystal. This situation has led to the development of a plethora of algorithms aimed at estimating IWC according to the equivalent reflectivity factor (e.g., Heymsfield et al., 2005; Hogan et al., 2006), giving rise to extensive discussions on the dependency of the accuracy of radar retrieved IWC with respect to the algorithm used. Uncertainties arise from the fact that both the size distribution and the particle scattering properties vary and are unknown in the in radar sample volume where IWC is retrieved. Consequently, some simplifying assumptions have to be made. Investigating the performance of retrievals considering the microphysical effects cannot be pursued only with the use of real data and an electromagnetic simulator of the radar response is an essential tool for performance evaluation, allowing sufficient detail to fully understand the contribution of each single effect on the processes involved. To simplify the complexity of the problem, the main assumption made in this study is that the ice particles can be represented by soft spheroids obtained from a mixture of air and ice (Petty and Huang, 2010; Liu, 2004; Heymsfield et al., 2018).

Concerning the *m-D* relation, the tuned parameters in $\mathrm{IWC}(\mathrm{PSD}\hat{\mathbf{p}}_{pp})$ given in Section 5 were used. The same 1-s *PSD*s used in the m-D relation tuning process were used to derive reflectivity factor and specific attenuation at the Ku-, Ka-, and W-band frequencies for an incident beam angle of 90^{o}. The procedure was based on T-matrix and Mueller-matrix scattering models, and, for the dielectric relation, the traditional Bruggeman mixing formula was used. The shape of all particles is defined by horizontally-aligned oblate spheroids with axial ratio equal to 0.6. As is well known, such modeling is obviously not an optimal proxy for all radars, as it is not able to fully represent the Ka- and W-band (Kneifel et al., 2011). At the same time, it is believed that no model (Leinonen and Moiseev 2015; Leinonen and Szyrmer 2015; Kuo et al. 2016) can simultaneously represent all the habits and even more the composition of those contained in a radar measurement volume.

The generic relationship between ice water content in unit of g/m^3 and the equivalent reflectivity factor in mm^6/m^3 is usually expressed by a power law

$$IWC\,(\xi_f) = \alpha_f \xi_f^{\beta_f} \qquad (17)$$

where α_f and β_f are constant coefficients for a given radar frequency (*f*).

Using a nonlinear regression analysis, it was possible to find the coefficients α_f and β_f by minimizing the differences between the measured EIWC in (14) and IWC estimate in (17) where both of them are derived from the same PSD. The first three rows of Table IV report the values of the optimized coefficients of (17) for the Ku- (*ue*), Ka- (*ae*), and W-bands (*we*), respectively. It is to be noted, that while the parameters α are fairly similar each other, the value of the exponents β increases as a function of the frequency.

The IWC-ξ algorithms are then applied to the entire reflectivity measurement dataset simulated from the PSDs collected for temperatures below zero to obtain their performance in terms of merit factors, as shown in Table V. All the three algorithms present practically zero NB values while NSE decreases with increasing frequency. The increase of ρ with frequency confirms that radars with high frequency are more sensitive to small ice crystals than those with low frequency.

For spherical raindrops, using DFR between two equivalent reflectivities as in (11), has allowed us to retrieve the drop median volume diameter that, together with the total raindrop concentration, and having fixed the shape parameter μ, univocally characterizes the DSD (Meneghini et al., 1997; Iguchi et al., 2000; Rose and Chandrasekar, 2006; Seto et al., 2013; Gorgucci and Baldini, 2016). In the presence of ice crystals it is not possible to unambiguously retrieve the size of the particles from DFR measurements because of the different habits that can exist in the cloud (e.g., Matrosov, 1998; Hogan et al., 2000; Liao et al., 2005). To this end, any assumption of habits in the radar sampling volume would be an arbitrary simplification. However, for particular conditions such as the case in which the habit does not present a wide variability, it remains valid that the DFR can be a suitable proxy of an average particle size contained in the radar sampling volume even if it is not possible to represent a relationship in a closed form. Bearing in mind of these considerations, DFR can be used as additional information for estimating IWC. Hence, the following relationship can be written

$$IWC_{poq}(DFR) = \alpha \xi_u^{\beta} DFR_{poq}^{\gamma} \qquad (18)$$

where α, β, and γ are constants and the subscript *poq* indicates that the reflectivity ratio is between reflectivities at the *p*- and the *q*-band, with the frequency of *p* greater than *q*. The following three reflectivity ratios were taken into account: $DFR_{aou}=\xi_a/\xi_u$, $DFR_{woa}=\xi_w/\xi_a$, and $DFR_{wou}=\xi_w/\xi_u$.

With the same approach used to optimize the coefficients in (17), the coefficients α, β, and γ of (18) were found for the three DFR relationships using the same tuned *m-D* algorithm. Table IV gives also the values of α, β, and γ for the three *aou*, *woa*, *wou* algorithms. It is immediate to note that the coefficients of *aou* and *woa* are quite similar and both very different from those of *wou*. Also in this case, to analyze the behavior of the different algorithms, they are applied to the simulated reflectivity measurements for which the temperature is below 0° C. The results are summarized in Table V. Also in this case, the merit factors are characterized by NBs close to zero. NSE of the *aou* algorithm takes a value close to those of *ue* and *ae* algorithms, while DFR algorithms using W-band measurements have the best performances. Again, it is evident that including W-band provides more precise information about IWC as highlighted by the ρ values.

Gaussiat et al. (2003) suggested the use of a triple-frequency radar to allow the estimation of two differential attenuations from which, in the presence of ice particles, the liquid water content could be estimated more accurately with respect to a dual-frequency radar. More recently, progress in characterizing the scattering of more realistic ice crystal shapes at microwave frequencies generated new expectations for triple-frequency radars. In particular, it has been clearly shown that in the DFR domain, defined by DFR_{aou} and DFR_{woa}, it is possible to obtain information capable of discriminating between different habits (Kulie et al., 2010; Kneifel et al., 2011; Leinonen et al., 2012).

An IWC algorithm that is a function of both DFR_{aou} and DFR_{woa} can be written as

$$IWC(DFR) = \alpha \xi_u^{\beta} \frac{DFR_{aou}^{\gamma}}{DFR_{woa}^{\delta}} \qquad (19)$$

where α, β, γ, and δ are the coefficients of the *2dfr* parameterization whose values, obtained with the same approach previously used to find (17) and (18), are reported in the last row of Table IV. The behavior of this algorithm is quantified by its merit factors (Table V) that present the best performances both with respect to SFR algorithms (17) and those that use the different DFRs as in (18).

The estimators defined by the equations (17), (18), and (19) can be written in compact form using the notation $\mathrm{IWC}(\mathrm{SRM}, \hat{\mathbf{p}}_{rm})$ where $\hat{\mathbf{p}}_{rm}$ is the optimized vector of coefficients α, β, γ, and δ obtained from simulated radar measurements (*rs*) which refer to the algorithms listed in Table IV, whereas SRM here means that the coefficients were applied to simulated radar measurements computed directly from measured PSDs.

Section 5 has shown that $\mathrm{IWC}(\mathrm{PSD}, \hat{\mathbf{p}}_{LI})$ relations respond differently to the variation of both the ambient temperature and the CWC. In particular, it has been observed that also the $\mathrm{IWC}(\mathrm{PSD}, \hat{\mathbf{p}}_{pp})$ with the coefficients found by the optimization between IWC and EIWC is outperformed by the $\mathrm{IWC}(\mathrm{PSD}^{ci}, \hat{\mathbf{p}}_{pp}^{ci})$ whose coefficients are optimized for the different CWC intervals (*ci*) and that the performances are different in the various CWC domains (Figs. 5).

In light of this result, it may be interesting to observe whether the $\mathrm{IWC}(\mathrm{SRM}, \hat{\mathbf{p}}_{rm})$ estimations obtained with relations based on reflectivity, shows a similar variability with the CWC. In this case, compatibly with the available data, new CWC class intervals have been defined as 1) CWC≤10^{-5} g/m^{-3}, 2) 10^{-5}<CWC≤10^{-3} g/m^{-3}, 3) 10^{-3}<CWC≤10^{-2} g/m^{-3}, 4) 10^{-2}<CWC≤10^{-1} g/m^{-3}, 5) CWC>0.1 g/m^{-3} and for each *ci* class interval, the $\hat{\mathbf{p}}_{rm}^{ci}$ parameters of (17), (18) and (19) were found.

Figures 6 display NSE, NB, and ρ of $\mathrm{IWC}(\mathrm{SRM}, \hat{\mathbf{p}}_{rm}^{ci})$ and $\mathrm{IWC}(\mathrm{SRM}^{ci}, \hat{\mathbf{p}}_{rm}^{ci})$. In general, it is clear that the merit factors show better values as the number of parameter used by the IWC algorithm increases. An aspect to underline concerns $\mathrm{IWC}(\mathrm{SRM}^{ci}, \hat{\mathbf{p}}_{rm}^{ci})$ (green lines) is that the classes with higher CWC have the worst merit factors. Another point to highlight is that among the multi-frequency algorithms, the one that uses DFR_{aou} exhibits a behavior similar to those based on reflectivity alone such as *ue* and *ae,* perhaps determined by the low ice discriminating power of the

Ku-band compared to the Ka- and W-band, whereas *we* algorithm is comparable to the performances of *woa*, *wou*, and *2dfr*. In conclusion, also in this case it appears that the merit factors of the algorithm obtained by composing the different $\mathrm{IWC}(\mathrm{SRM}, \hat{\mathbf{p}}_{rm}^{ci})$ (black line) are much better than those of $\mathrm{IWC}(\mathrm{SRM}, \hat{\mathbf{p}}_{rm})$ (magenta line) and also that the best algorithm for estimating IWC is *2dfr* although those based on W-band, namely: *we*, *woa* and *wou*, do not have too much worse performances.

7. Experimental evaluation of IWC radar algorithms

To evaluate the behavior of the $\mathrm{IWC}(\mathrm{SRM}, \hat{\mathbf{p}}_{rm})$ algorithms, collocated measurements from the APR3 triple frequency radar on board the DC-8 aircraft and in-situ microphysical measurements and EIWC measurements provided by the Citation aircraft were used. The APR-3 provides measured profiles of Zu_m, Za_m, and Zw_m (i.e., $Z = 10\log_{10}\xi$) at the Ku- (13 GHz), Ka- (35 GHz), and W-band (94 GHz) frequencies, respectively. Each profile consists of range gates spaced 30 m apart.

In a rigorous way, the comparison between collocated measurements should be made when, for a fixed time, the measurements collected by the two aircrafts are referred ideally to the same, uniformly filled, sampling volume. However, imposing such a condition would result in a small number of coinciding measurements in time and space and the resulting data set would not be statistically significant. This limitation forces us to relax the definition of space-time collocation by expanding the search domain for the collocated matchings. Consequently, the measurements will not result exactly collocated and a decrease of the correlation coefficient, with respect to what was obtained using simulations, is expected. Following Heymsfield et al. (2018), the collocation rule we applied defines the collocated measurement domain as made up of aircraft observations that are separated in a time of less than 300 s and terms of horizontal distance defined at the altitude of flight of the Citation of less than 2 km. Among the measurements satisfying these two conditions, the one with the smallest time shift was chosen for subsequent analysis. The remaining measurements that comply with the collocation rule mentioned above are used to quantify the measurements gradient within the colocation domain. For example, Fig. 7 shows the distribution of the reflectivity factor gradient at Ku band defined as the max-min values of Zu_m within each collocated domain for each matching found. The reflectivity factor gradient quantifies in some way the variability experienced in the collocation domain and gives an idea of the validity of the uniformity hypothesis of the observed field in that domain.

The reflectivity measurements of a triple-frequency radar are relatively affected by path attenuation depending mainly on the frequency used. Past studies have shown that ice does not produce a significant attenuation up to the Ku-band; conversely, at Ka-band attenuation due to ice may be not negligible while at the W-band it can be noticeable. It follows that to assess the behavior of the different IWC algorithms, the cumulative attenuation needs to be accounted for.

It is well known that attenuation correction with iterative methods is inherently unstable since any bias propagates through the propagation path, making it necessary to constrain somehow the total attenuation (Meneghini et al. 2000). This effect could be much more pronounced in the presence of ice particles because it is difficult to express a relationship for the attenuation correction due to its strong variability with the different types of habits present in clouds. To overcome this limitation in a reasonable way, we assume the Ku-band to be marginally affected by path attenuation in ice, so that we can assume $Zu_e=Zu_m$, where the subscript "e" indicates the effective refelectivity, and use it as a reference to compensate the attenuation effects for Za_m and Zw_m (Kulie et al. 2014; Leinonen et al., 2018).

The entire PSD dataset obtained from in-situ measurements was used to simulate Zu, Za, and Zw with the corresponding specific attenuations in dB/km. For the simulations of the reflectivity factor, particle density is needed instead of mass because the former drives the particle's volume fraction of air and ice, thus modifying the particle's refractive index, which in turns modifies the back-scattering cross-section properties that are strictly related to the reflectivity factor. However, particle's mass and density are related through the particle's volume, which in our simplified case coincides with that of an oblate spheroid. For each increment of 0.1 dB in Zu reflectivity, the corresponding mean values of the specific attenuations a_a and a_w, for Ka- and W-band respectively, were found.

Fig. 8 shows the resulting specific attenuations a_a and a_w as a function of Zu. With these values, it was possible from a given measured Zu profile to reconstruct the corresponding profile of cumulated attenuation at the Ka- and W-band to get Za_e and Zw_e from Za_m and Zw_m. The average attenuation correction of the collocated reflectivity measurements was 0.19 dB and 1.45 dB for the Ka- and W-bands, respectively.

It was thus possible to create the collocated domain consisting of the EIWC measurements and radar measurements for performance evaluation of the different IWC radar algorithms, given in Table IV, with collected radar measurements (CRM). The behavior of the $\mathrm{IWC}(\mathrm{SRM}, \hat{\mathbf{p}}_{rm})$ merit factors for this dataset is shown in Fig. 9, and consists of both a generalized increase of NSE in comparison with Fig. 6a (magenta line), and a peculiar increasing trend, as the number of parameters used by the algorithms grows, that appears to contradict what is depicted in Fig. 6a. Considering the many assumptions made in deriving the algorithms, such as the hypothesis that ice crystals can be described by soft spheres and have a fixed temperature of -10º C, the NSE increase is not surprising. The trend can be explained by the fact that the reflectivity measurements are subject to independent measurement errors and consequently the increase in the number of parameters used by the algorithm increases the influence of measurement errors on the IWC estimate. As far as NB is concerned, it does not present particular variations with respect to what shown in Fig. 6b, remaining almost close to zero. A significant reduction is also presented by ρ with a slightly decreasing trend passing from 0.39 of the algorithm *ue* to 0.26 of *2dfr* presenting a maximum value for *aou* (0.46) and a minimum for *woa* (0.13). Obviously, the reduction can be influenced by how much the collocated measurements are affected by reflectivity gradients. About the low *woa* value, it must be underlined that it depends on two measurements that both undergo the correction for attenuation.

With this significant increase of the measurement errors, along with the consequent decrease of the correlation between the $\mathrm{IWC}(\mathrm{SRM}, \hat{\mathbf{p}}_{rm})$ estimates and the EIWC, it can be interesting to check whether CWC is still able to discriminate between the different situations highlighted in the simulations, as illustrated above in Figs. 7.

Using actual radar measurements to compute $\mathrm{IWC}(\mathrm{CRM}^{ci}, \hat{\mathbf{p}}_{rm}^{ci})$ with coefficients derived in simulations optimized to CWC class intervals, merit factors for each single class *ci* and the composition of $\mathrm{IWC}(\mathrm{SRM}^{ci}, \hat{\mathbf{p}}_{rm}^{ci})$ were found. Although NSE (Fig. 10a), NB (Fig. 10b), and ρ (Fig. 10c) show a strong variability between the different CWC intervals, the composition of $\mathrm{IWC}(\mathrm{SRM}^{ci}, \hat{\mathbf{p}}_{rm}^{ci})$ has better performances than the single algorithm $\mathrm{IWC}(\mathrm{SRM}, \hat{\mathbf{p}}_{rm})$.

Although an operational measure of the CWC is not currently possible and therefore it is unrealistic to use the IWC algorithms optimized to its value, the analysis highlights that using CWC allow to provide better estimates than those obtained with a single algorithm, regardless of CWC, even in the presence of significant measurement errors.

8. A new look at the DFR domain

The comparison of merit factors of Figs. 10, obtained using the reflectivity data collected by the APR3, and those shown in Figs. 6, obtained using the simulated reflectivities, clearly shows that the DFR measurements are affected by measurement errors to such an extent that nullify the benefits brought by using multiparametric algorithms. Actually, if Figs. 6 show the better performance of the multiparametric algorithms in a synthetic error-free scenario, Figs. 10 depict, in a more realistic case, worse performances as the number of parameters used in algorithms increases.

For this reason, we need to analyze more deeply the characteristics of the DFR domain and its behavior for varying meteorological and microphysical parameters. Considering the DFR domain defined by the dual frequency ratio pairs (DFR_{woa}, DFR_{aou}) in logarithmic scale, Fig. 11 shows the scatterplot obtained by reflectivity measurements collected by the APR3 with temperatures below the freezing level for which the collocated CWC, relative humidity, and dewpoint measurements are also available (10021 observations). Moreover, in Fig. 11, overlaid for reference, some curves obtained by the triple-frequency calculations for various ice particle scattering models by Kulie et al. (2014) are displayed. Readers can refer to this paper for more details about the definitions of the acronyms of each model and on the various ice particle scattering involved.

The main information that can be obtained from Fig. 11 is related to the large variability that affects the DFR measurements, that depends mainly on measurement errors (signal fluctuations, attenuation, radar calibration, reflectivity gradients) and the large variety of ice crystal habits into the radar volume. This large spread does not allow to identify any particular specific model trends except the large cluster of points in the low part of the domain that is common to all the models. This is experimentally supported by the large amount of in situ measurements performed with the cloud particle imager (CPI) habit observations (Bailey and Hallett, 2009) which reports the wide variety of the ice crystal habits that is further enriched with their many irregularities and imperfections making, somewhat unlikely, that a radar volume can be filled exclusively with a single type of ice crystal habit. It follows that the corresponding scattered signal cannot be described using a single particle-backscattering model. Therefore, although different ice habits in the cloud have contributed to the composition of the resulting reflectivity, using experimental measurements to recognizing them from specific DFR signatures appears quite difficult.

In the previous sections it was found that the quantity of supercooled drops plays an important role in the characterization of ice crystals as it modulates the degree of riming. To explore whether this feature can be revealed in the DFR domain, one can look at the domain from another point of view by considering the following approach. The entire variability range of CWC values has been divided into three class intervals such as they roughly represent the dry (d), the moist (m) and the wet (w) environment that are bounded by the following thresholds: d) $<10^{-4}$ g/m^{-3}, m) from 10^{-4} to 10^{-2} g/m^{-3} and w) $> 10^{-2}$ g/m^{-3}. These thresholds generate three DFR classes such that all the (DFR_{aou}, DFR_{woa}) pairs of a class have a corresponding CWC value belonging to only one of the three intervals. The classes are quite consistent in that they contain a sufficient number of DFR pairs equal to 3028 (d), 4073 (m), and 2920 (w). Their scatterplots are characterized by having the slopes of the least squares regression line through origin of 0.469, 0.424, and 0.361 with correlation coefficients of 0.1077, 0.1664, and 0.2380, respectively. These results lead to two immediate considerations regarding the relationship between the DFR_{woa} and DFR_{aou}. The first one is that these scatterplots, although subjected to a high degree of variability, allow to observe a decreasing trend of the slope as the CWC increases. The second one, despite being supported by very small values, refers to the increasing trend of the correlation coefficient as the CWC increases.

The contradictory nature of the results depicted in Figs. 10 with respect to those in Figs. 6 can be linked to the fact that the latter was obtained using measurements obtained from the same electromagnetic and microphysical models on which the algorithms were found while Fig. 10 was obtained by applying the aforementioned algorithms to the real radar measurements.

The limitations associated with the assumption of a predefined electromagnetic and microphysical model can be partially overcome by using the algorithm parameters (11), (12), and (13) directly obtained from a nonlinear regression analysis applied to the collected radar measurements, in the framework of the DFR domain.

If we want to take advantage of the improvements made possible by the use of the CWC on the estimate of the IWC, it is necessary to replace it with a parameter that can be obtained directly from the radar measurements. For this purpose, the slopes of the two external classes *dry* and *wet* were used to generate three classes of (DFR_{aou}, DFR_{woa}) pairs, corresponding to the three CWC classes. By considering the slope parameter *Sl* defined as

$$Sl = \frac{\log_{10}\left(DFR_{aou}\right)}{\log_{10}\left(DFR_{woa}\right)} \tag{20}$$

each DFR pair will be associated with a value of *Sl* and will, therefore, be assigned to one of the three slope class intervals - *dry* (>0.469), *moist* (from 0.469 to 0.361) and *wet* (<0.361). In this framework, the $\mathrm{IWC}(\mathrm{CRM}\hat{\mathbf{p}}_{dfr})$ relations for the entire DFR domain and the $\mathrm{IWC}(\mathrm{CRM}^{\mathrm{slp}},\hat{\mathbf{p}}_{dfr}^{\mathrm{slp}})$, where the superscript *slp* refers to the radar measurements generating DFR pairs belonging to the class *slp*, were found by the optimization between IWC estimates and EIWC. The vector coefficients $\hat{\mathbf{p}}_{dfr}$ and $\hat{\mathbf{p}}_{dfr}^{\mathrm{sl}}$ are given in Table VI and Tables VII, VIII, IX, respectively.

The result of the analysis is summarized in Figs. 12 where the merit factors related to the dry, moist, and wet classes are depicted versus the different algorithms. The NSE of Fig. 12a shows a noticeable improvement compared to the correspondent of Fig. 10a as expected, along with the non-increasing trends of NSE with the number of used parameters. However, the really important result achieved is that starting from CWC intervals, it is possible to obtain thresholds in the DFR domain such that for each ($\mathrm{DFR}_{\mathrm{aou}}$, $\mathrm{DFR}_{\mathrm{woa}}$) pair it is possible to calculate the slope parameter *Sl* that selects one between the dry, moist, or wet class and then the corresponding algorithm to get.

This method allows us to obtain from the composition of $\mathrm{IWC}(\mathrm{CRM}^{\mathrm{slp}}, \hat{\mathbf{p}}^{\mathrm{slp}}_{dfr})$ relations an NSE which is definitely better for all the algorithms than that obtained using $\mathrm{IWC}(\mathrm{CRM}, \hat{\mathbf{p}}_{dfr})$, a result that could be obtained by knowing the CWC. This surprising result is further confirmed by Fig 12c, where ρ of the composite function are much better, albeit overall lower, for all the multi-frequency algorithms, than the ρ showed by the single relationship.

9. Summary and conclusions

The main objective of this study was to analyze the IWC estimate in a context of single and multiple frequency radars to examine at what extent multi-frequency radar contributes to its improvement. The study was performed by extracting from the high-quality dataset acquired during the OLYMPEX campaign, a selected dataset composed of airborne triple-frequency radar observations (Ku-, Ka-, and W-band) in combination with in-situ microphysical and meteorological measurements.

In the absence of reliable CSI measurements, a first problem to solve was to establish how to obtain trustworthy IWC measurements in cloud to be compared with different radar estimates. The best choice, among the measurements available, was the joint use of the TWC collected by the Nevzorov probe with the LWC measured by the King probe whose difference (named EIWC) was assumed as the reference IWC. For a comprehensive characterization of the cloud environment, meteorological measurements such as air temperature, relative humidity, and frost point temperature were used, while the condition for riming were related to CWC measurements.

The performance of the $\mathrm{IWC}(\mathrm{PSD}, \mathrm{p}_{LI})$ estimators and their variability with temperature and CWC suggested to develop an algorithm $\mathrm{IWC}(\mathrm{PSD}, \hat{\mathbf{p}}_{pp})$ tuned on the whole campaign data and a set of specific algorithms $\mathrm{IWC}(\mathrm{PSD}, \hat{\mathbf{p}}_{\mathrm{pp}}^{\mathrm{ci}})$ tuned on the different CWC class intervals. By varying CWC class intervals the parameters defining the m-D relationship appeared to be related to each other and such relation was expressed with a third-degree polynomial function.

Using a procedure based on T-matrix and Mueller-matrix scattering models, from the same PSD dataset, reflectivity factor and specific attenuation at the Ku-, Ka-, and W-band frequencies were simulated assuming horizontally-aligned oblate spheroids with axial ratio equal to 0.6. Employing a nonlinear regression analysis, IWC radar algorithms were obtained minimizing the differences between their estimates and the corresponding EIWC measurements.

The algorithms examined are based both on the single parameter of reflectivity and the combined use of the Ku-band reflectivity with the dual frequency ratios DFR_{aou}, DFR_{woa}, DFR_{wou}, and DFR_{aou} jointly with DFR_{woa}. The performance of the different algorithms improved as the number of parameters increase, except for DFR_{aou}. However, the most interesting result was that the merit factors obtained by the composition of algorithms optimized for the different CWC class intervals are distinctly better than the corresponding ones of a single algorithm, applied regardless of the CWC value, both in terms of NSE and ρ.

For an assessment in an operational context, collocated measurements collected by the APR3 radar were used jointly with microphysical and meteorological parameters. For each PSD measurement, the Ku reflectivity was simulated and the corresponding specific attenuations at the Ka- and W-band were simulated as well and a relationship allowing to obtain, for a fixed Ku reflectivity value, the average specific attenuations of the other two bands. Assuming the Ku-band reflectivity measurements as non-attenuated by ice particles, they were used for determining the relative specific attenuations to correct the reflectivity measurements of the other two bands.

The analysis of the performance of the different algorithms, using collected radar measurements as input, was also carried out computing both $\mathrm{IWC}(\mathrm{SRM}, \hat{\mathbf{p}}_{rm})$ and

$\mathrm{IWC}(\mathrm{SRM}^{\mathrm{ci}}, \hat{\mathbf{p}}^{\mathrm{ci}}_{\mathrm{rm}})$. The evaluation of the different algorithms highlighted two very interesting aspects. The first is that the merit factors - NSE, NB, and ρ - of $\mathrm{IWC}(\mathrm{SRM}, \hat{\mathbf{p}}_{rm})$ behaves worse than the ones obtained with the composition of $\mathrm{IWC}(\mathrm{SRM}^{\mathrm{ci}}, \hat{\mathbf{p}}^{\mathrm{ci}}_{\mathrm{rm}})$ for all the different radar IWC algorithms. The second aspect is that all the merit factors are worse than the correspondents obtained using the simulated measurements. However, this was expected as the modeling hypotheses underlying the simulation could not correctly reproduce the reality. A further source of errors is determined by the space-time domain chosen to define collocated measurements and in particular by the reflectivity gradients present in it as well as by the measurement errors. However, an aspect to underline is that in general the correlation between the EIWC and its estimates decreases using the DFR algorithms, highlighting a not negligible variability of the DFR parameter.

To focus on this aspect, the domain defined by the (DFR_{woa}, DFR_{aou}) pairs was considered to find a substitute for CWC, being CWC not an operational measurement and, therefore, not practically usable. Compatibly with the sample size of (DFR_{aou}, DFR_{woa}) pairs in the different regions of the domain, three CWC class intervals called *dry*, *moist*, and *wet* were chosen. It was observed that the scatter of the corresponding pairs in each class interval had the slope of least square line of increasing value with decreasing CWC. These values were taken to define three class intervals of the *Sl* parameter defined by the ratio between DFR_{aou} and DFR_{woa}.

For a more realistic analysis that does not require any a priori assumptions about the models needed for simulating reflectivity measurements, real radar measurements and in-situ microphysical observations were jointly used. The advantage of this approach lies in the fact that it does not involve assumptions about the particle size distributions, the statistical relationship between crystal mass and maximum dimension, or the wavelength-dependent backscatter cross-section variability. On the contrary, challenges are posed by the proper matching of radar and microphysical measurements in the space-time domain, along with attenuation corrections and calibration errors.

Using collocated radar and PSD measurements, parameterizations of radar IWC algorithms (17), (18), and (19) were found. The interesting result to be underlined is that from the comparative analysis of the merit factors of $\mathrm{IWC}(\mathrm{CRM}, \hat{\mathbf{p}}_{dfr})$, i.e. with parameters obtained using all the data available, and the IWC estimated by the composition of $\mathrm{IWC}(\mathrm{CRM}^{\mathrm{slp}}, \mathrm{p}_{\mathrm{dfr}}^{\mathrm{slp}})$ with the parameters obtained for the three slope class intervals, the latter has much better merit factors of all the algorithms considered. Furthermore, the algorithms that use the DFR parameters do not present worse merit factors than SFR algorithm. This can mean that the major contribution to the error of the DFR-based algorithms, shown in Figs 11, are not DFR fluctuation measurements but also to systematic errors (radar calibration).

In conclusion, the study highlighted that it is possible to divide the DFR domain into classes such that for a (DFR_{woa}, DFR_{aou}) pair it is possible to find a slope value *slp* to select a set of $\mathrm{IWC}(\mathrm{CRM}^{\mathrm{slp}}, \mathrm{p}_{\mathrm{dfr}}^{\mathrm{slp}})$ whose compositions present estimates with merit factors better than the ones get with $\mathrm{IWC}(\mathrm{CRM}, \hat{\mathbf{p}}_{dfr})$ for all the algorithms. Obviously, as the classes increase, better estimates will correspond anyway, but to obtain this further improvement it will be necessary to reduce measurement errors.

Acknowledgments.

This work has been partially supported by the European Space Agency, ESA Contract No. 4000125959/18/NL/NA. OLYMPEX datasets used in this paper are available online from the NASA EOSDIS Global Hydrology Resource Center Distributed Active Archive Center, Huntsville, Alabama, U.S.A., (https://earthdata.nasa.gov/eosdis/daacs/ghrc). The authors acknowledge the international cooperation established within the GPM Ground Validation Program. Finally, the authors acknowledge HIMET s.r.l. (L'Aquila, Italy) for collaborative support, data analysis, and manuscript preparation.

References

Abel, S. J., Cotton, R. J., Barrett, P. A. and Vance, A. K. 2014: A comparison of ice water content measurement techniques on the FAAM BAe-146 aircraft. Atmospheric Measurement Technology, 7, 3007 – 3022.

Bailey M., and Hallett J., 2009. A comprehensive habit diagram for atmospheric ice crystals: confirmation from the Laboratory, AIRS II, and Other Field Studies. J. Atmos. Sci., 66, 2888–2899.

Barros, A. P., and Coauthors, 2014: NASA GPM-ground validation: Integrated Precipitation and Hydrology Experiment 2014. NASA Tech. Rep., 64 pp.,Borque, P., Harnos, K., Nesbitt, S. W. and McFarquhar, G. M. 2019: Improved parameterization of ice particle size distributions using uncorrelated mass spectrum parameters: Results using GCPEX. J. Appl. Meteor. Climatol., 58, 1657–1676.

Botta, G., Aydin, K., Verlinde, J., Avramov, A. E., Ackerman, A. S., Fridlind, A. M., McFarquhar, G. M., Wolde, M., 2011. Millimeter wave scattering from ice crystals and their aggregates: Comparing cloud model simulations with X- and Ka-band radar measurements. J. Geophys. Res. 116, D00T04.

Brandes, E. A., Ikeda, K., Zhang, G., Schönhuber, M., Rasmussen, R. M., 2007. A statistical and physical description of hydrometeor distributions in Colorado snowstorms using a video disdrometer. J. Appl. Meteor. Climatol. 46, 634–650.

Brown, P. R. A., Francis P. N., 1995. Improved measurements of the ice water content in cirrus using a total-water probe. J. Atmos. Oceanic Technol. 12, 410–414.

Chase, R. J., Finlon, J. A., Borque, P., McFarquhar, G. M., Nesbitt, S. W., Tanelli, S., Sy, O. O., Durden, S. L. and Poellot, M. 2018: Evaluation of triple-frequency radar retrieval of snowfall properties using coincident airborne in situ observations during OLYMPEX. Geophys. Res. Lett., 45, 5752 – 5760.

Delanoë, J., Protat A., Testud, J., Bouniol, D., Heymsfield, A. J., Bansemer, A., Brown, P. R. A., Forbes, R. M., 2005. Statistical properties of the normalized ice particle size distribution. J. Geophys. Res., 110, D10201.

Field, P. R., Heymsfield, A. J., Bansemer A., 2007. Snow size distribution parameterization for midlatitude and tropical ice clouds. J. Atmos. Sci., 64, 4346–4365.

Field, P., and Heymsfield, A. J. , 2015. Importance of snow to global precipitation. Geophys. Res. Lett., 42, 9512–9520.

Gaussiat, N., Sauvageot H., and Illingworth, A. J., 2003. Cloud liquid water and ice content retrieval by multiwavelength radar, J. Atmos. Oceanic Technol., 20, 1264–1275.

Giangrande, S. E., Toto T., Bansemer A., Kumjian M. R., Mishra S., and Ryzhkov A. V., 2016. Insights into riming and aggregation processes as revealed by aircraft, radar, and disdrometer observations for an 27 April 2011 widespread precipitation event. J. Geophys. Res. Atmos., 121, 5846–5863.

Gorgucci E., Baldini, L., 2016. A self-consistent numerical method for microphysical retrieval in rain using GPM dual-wavelength radar. J. Atmos. Oceanic Technol. 33, 2205–2223.

Heymsfield, A. J., 1982. A comparative study of the rates of development of potential graupel and hail embryos in High Plains storms. J. Atmos. Sci., 39, 2867–2897.

Heymsfield, A. J., Bansemer, A., Field, P. R., Durden, S. L., Stith, J. L., Dye, J. E., Hall, W., Grainger, C. A., 2002. Observations and parameterizations of particle size distributions in deep tropical cirrus and stratiform precipitating clouds: Results from in situ observations in TRMM field campaigns. J. Atmos. Sci., 59, 3457–3491.

Heymsfield, A. J., 2003. Properties of tropical and midlatitude ice cloud particle ensembles. Part I: Median mass diameters and terminal velocities. J. Atmos. Sci. 60, 2573–2591.

Heymsfield, A. J., Bansemer, A., Schmitt C., Twohy, C., Poellot M. R., 2004. Effective ice particle densities derived from aircraft data. J. Atmos. Sci. 61, 982–1003.

Heymsfield, A. J., Wang Z., Matrosov, S., 2005. Improved radar ice water content retrieval algorithms using coincident microphysical and radar measurements. J. Appl. Meteor., vol. 44, 1391-1412.

Heymsfield, A. J., Schmitt C., Bansemer, A., Twohy C. H., 2010. Improved representation of ice particle masses based on observations in natural clouds. J. Atmos. Sci., 67, 3303–3318.

Heymsfield A. J., Schmitt C., and Bansemer, A., 2013. Ice cloud particle size distributions and pressure-dependent terminal velocities from in situ observations at temperatures from 0^{o} to –86^{o}C. J. Atmos. Sci., 70, 4123–4154.

Heymsfield, A. J., Bansemer, A., Poellot M. R., Wood N., 2015. Observations of ice microphysics through the melting layer. J. Atmos. Sci., 72, 2902–2928.

Heymsfield, A. J., Bansemer, A., Wood N. B., Liu G., Tanelli, S., Sy, O. O., Poellot, M., Liu, C., 2018. Toward improving ice water content and snow-rate retrievals from radars. Part II: Results from three wavelength radar–collocated in situ measurements and CloudSat–GPM–TRMM Radar Data. J. Appl. Meteorol. Climatol. 57, 365–389.

Hogan, R. J., Illingworth, A. J., and Sauvageot, H., 2000. Measuring crystal size in cirrus using 35- and 94-GHz radars. J. Atmos. Ocean. Tech. 17, 27–37.

Hogan, R. J., Mittermaier M. P., Illingworth A. J., 2006. The retrieval of ice water content from radar reflectivity factor and temperature and its use in evaluating a mesoscale model. J. Appl. Meteor. Climatol. 45, 301–317.

Hogan, R. J., Westbrook C. D., 2014. Equation for the microwave backscatter cross section of aggregate snowflakes using the self-similar Rayleigh–Gans approximation. J. Atmos. Sci. 71, 3292–3301.

Houze, R. A., McMurdie, L. A., Peterson, W. A., Schwaller, M. R., Baccus, W., Lundquist, J., Mass, C., Nijssen, B., Rutledge, S. A., Hudak, D., Tanelli, S., Mace, G. G., Poellot, M., Lettenmaier, D., Zagrodnik, J., Rowe, A., Dehart, J., Madaus, L. & Barnes, H., 2017. The

Olympic Mountains Experiment (OLYMPEX). *Bulletin of the American Meteorological Society*, 98, 2167 – 2188.

Iguchi, T., Kozu T., Meneghini, R., Awaka J., Okamoto K., 2000. Rain-profiling algorithm for the TRMM precipitation radar. J. Appl. Meteor. 39, 2038–2052.

Jensen, M. P., and Coauthors, 2016: The Midlatitude Continental Convective Clouds Experiment (MC3E). Bull. Amer. Meteor. Soc., 97, 1667–1686.

Kingsmill, D. E., Yuter S. E., Heymsfield A. J., Hobbs P. V., Korolev A. V., Stith J. L., Bansemer A.,. Haggerty J. A., and Rangno A. L., 2004. TRMM common microphysics products: A tool for evaluating spaceborne precipitation retrieval algorithms. J. Appl. Meteor. 43, 1598–1618.

Kneifel, S., Kulie M. S., Bennartz R., 2011. A triple-frequency approach to retrieve microphysical snowfall parameters. J. Geophys. Res. 116, D11203.

Korolev, A. V., Strapp J. W., Isaac G. A., and Nevzorov A. N., 1998. The Nevzorov airborne hot-wire LWC–TWC probe: Principle of operation and performance characteristics. J. Atmos. Oceanic Technol. 15, 1495–1510.

Korolev, A. V., Strapp, J.W., Isaac, G. A., and Emery, E., 2013: Improved airborne hot-wire measurements of ice water content in clouds, J. Atmos. Ocean. Tech., 30, 2121–2131.

Kulie, M.S., Bennartz R., Greenwald T., Chen Y., Wenig F., 2010. Uncertainties in microwave optical properties of frozen precipitation: Implications for remote sensing and data assimilation. J. Atmos. Sci. 67, 3471-3487.

Kulie, M. S., Hiley M. J., Bennartz R., Kneifel. S., Tanelli, S., 2014. Triple-frequency radar reflectivity signatures of snow: Observations and comparisons with theoretical ice particle scattering models, J. Appl. Meteorol. Climatol. 53, 1080–1098.

Kuo, K.-S., Olson, W. S., Johnson, B. T., Grecu, M., Tian, L., Clune, T. L., van Aartsen, B. H., Heymsfield, A. J., Liao, L., Meneghini, R., 2016. The microwave radiative properties of falling snow derived from nonspherical ice particle models. Part I: An extensive database of simulated pristine crystals and aggregate particles, and their scattering properties. J. Appl. Meteorol. Clim. 55, 691–708.

Lawson, R. P., O'Connor D., Zmarzly P., Weaver K., Baker B., Mo Q., Jonsson H., 2006. The 2D-S (stereo) probe: Design and preliminary tests of a new airborne, high-speed, high-resolution particle imaging probe. J. Atmos. Oceanic Technol. 23, 1462–1477.

Leinonen, J., Kneifel, S., Moisseev, D., Tyynelä, J., Tanelli, S., and Nousiainen, T., 2012. Evidence of nonspheroidal behavior in millimeter-wavelength radar observations of snowfall. J. Geophys. Res. 117, D18205.

Leinonen, J., Moisseev, D., 2015. What do triple-frequency radar signatures reveal about aggregate snowflakes? J. Geophys. Res. 120, 229–239.

Leinonen, J., Szyrmer, W., 2015. Radar signatures of snowflake riming: A modeling study. Earth Space Sci. 2, 346–358.

Leinonen, J., Lebsock M. D., Tanelli, S., Sy O. O., Dolan B., Chase R. J., Finlon J. A., von Lerber A., and Moisseev D., 2018. Retrieval of snowflake microphysical properties from multifrequency radar observations. Atmos. Meas. Tech. 11, 5471–5488.

Liao, L., Meneghini, R., Iguchi, T., Detwiler, A., 2005. Use of dualwavelength radar for snow parameter estimates. J. Atmos. Ocean. Tech. 22, 1494–1506.

Liao, L., Meneghini, R., Tokay A., Bliven L. F., 2016. Retrieval of snow properties for Ku- and Ka-band dual-frequency radar. J. Appl. Meteorol. Climatol. 55, 1845–1858.

Liu, G., 2004. Approximation of single scattering properties of ice and snow particles for high microwave frequencies. J. Atmos. Sci. 61, 2441–2456.

Liu, G., 2008. A database of microwave single-scattering properties for nonspherical ice particles. Bull. Amer. Meteor. Soc. 89, 1563–1570.

Matrosov, S. Y., 1998. A dual-wavelength radar method to measure snowfall rate. J. Appl. Meteorol. 37, 1510–1521.

Matrosov, S. Y., Heymsfield, A. J., Wang Z., 2005. Dual-frequency radar ratio of nonspherical atmospheric hydrometeors. Geophys. Res. Lett. 32, L13816.

Meneghini, R., Kumagai H., Wang J. R., Iguchi T., and Kozu T., 1997. Microphysical retrievals over stratiform rain using measurements from an airborne dual-wavelength radar-radiometer. IEEE Trans. Geosci. Remote Sens. 35, 487–506.

Meneghini, R., T. Iguchi, T. Kozu, L. Liao, K. Okamoto, J. A. Jones, and J. Kwiatkowski, 2000. Use of the Surface Reference Technique for path attenuation estimates from the TRMM Precipitation Radar. J. Appl. Meteor., 39, 2053–2070.

McFarquhar, G. M., Zhang G., Poellot M. R., Kok G. L., McCoy R., Tooman T., Fridlind A., Heymsfield, A. J., 2007. Ice properties of single-layer stratocumulus during the Mixed-Phase Arctic Cloud Experiment: 1. Observations. J. Geophys. Res. 112, D24201.

McFarquhar, G. M., Um J., Jackson R. C., 2013. Small cloud particle shapes in mixed-phase clouds. J. Appl. Meteor. Climatol. 52, 1277–1293.

Ni, X, Liu C., Zipser E., 2019: Ice microphysical properties near the tops of deep convective cores implied by the GPM dual-frequency radar observations. J. Atmos. Sci. 76, 2899-2917.

Ori, D., Maestri T., Rizzi R., Cimini D., Montopoli M., Marzano F. S., 2014. Scattering properties of modeled complex snowflakes and mixed-phase particles at microwave and millimeter frequencies. J. Geophys. Res. 119, –9947.

Petty, G. W., Huang W., 2010. Microwave backscatter and extinction by soft ice spheres and complex snow aggregates. J. Atmos. Sci. 67, 769-787.

Rose, C. R., Chandrasekar V., 2006. A GPM dual-frequency retrieval algorithm: DSD profile-optimization method. J. Atmos. Oceanic Technol. 23, 1372–1383.

Sadowy, G. A., Berkun A. C., Chun W., Im E., Durden S. L., 2003. Development of an advanced airborne precipitation radar. Microwave Journal, 46, 84-93.

Seto, S., Iguchi T., Oki T., 2013. The basic performance of a precipitation retrieval algorithm for the Global Precipitation Measurement mission's single/dual-frequency radar measurements. IEEE Trans. Geosci. Remote Sens. 51, 5239–5251.

Skofronick-Jackson, G., and Coauthors, 2015. Global Precipitation Measurement Cold Season Precipitation Experiment (GCPEX). Bull. Amer. Meteor. Soc. 96, 1719–1741.

Stephens, G. L., 2005. Cloud feedback in the climate system: A critical review. J. Clim. 18, 237-273.

Sy, O. O., and Coauthors, 2020: Impact of Mass–Size Parameterizations of Frozen Hydrometeors on Microphysical Retrievals: Evaluation by Matching Radar to In Situ Observations from GCPEx and OLYMPEx. J. Atmos. Oceanic Technol., 37, 993–1012.

Szyrmer, W, Zawadzki I., 2010. Snow studies. Part II: Average relationship between mass of snowflakes and their terminal fall velocity. J. Atmos. Sci. 67, 3319-3334.

Tanelli, S., Durden S. L., Im, E., 2006. Simultaneous measurements of Ku- and Ka-band sea surface cross-sections by an airborne radar. IEEE Geoscience and Remote Sensing Letters, 3(3), 359-363.

Testud, J., Oury S., Black R. A., Amayenc P., Dou X. K., 2001. The concept of ''normalized'' distribution to describe raindrop spectra: A tool for cloud physics and cloud remote sensing. J. Appl. Meteorol. 40, 1118– 1140.

Tridon, F., Battaglia A., Chase R. J., Turk F. Leinonen J. J., Kneifel S.; Mroz K., Finlon J., Bansemer A, Tanelli S., Heymsfield A. J., Nesbitt S. J., 2019. The microphysics of stratiform precipitation during OLYMPEX: Compatibility between triple-frequency radar and airborne in situ observations. J. Geophys. Res. Atmos., 124, 8764-8792.

Twohy, C. H., Schanot A. J., and Cooper W. A., 1997. Measurement of condensated water content in liquid and ice clouds using an airborne counterflow virtual impactor. J. Atmos. Oceanic Technol. 14, 197–202

Tyynelä, J., Leinonen, J. Moisseev D., Nousiainen T., 2011. Radar backscattering from snowflakes: Comparison of fractal, aggregate, and soft spheroid models, J. Atmos. Oceanic Tech., 28, 1365–1372.

Tyynelä, J., Chandrasekar V., 2014. Characterizing falling snow using multifrequency dual-polarization measurements, J. Geophys. Res. Atmos., 119, 8268–8283.

Ulbrich, C. W., 1983. Natural variations in the analytical form of raindrop size distributions. J. Climate Appl. Meteor. 22, 1764–1775.

Williams, C., Bringi, V., Carey, L., Chandrasekar, V., Gatlin, P., Haddad, Z., Munchak, S., Petersen, W., Meneghini, R., Nesbitt, S., Tanelli, S., Tokay, A., Wilson, A., Wolff, D., 2014. Describing the shape of raindrop size distributions using uncorrelated raindrop mass spectrum parameters. J. Appl. Meteor. Climatol. 53, 1282–1296.

TABLE I - Coefficients a and b of the power law relation m-D (13). $\mathbf{p}_{LI}$ *is the label that identifies the different literature parametrizations.*

$\mathbf{p}_{LI}$	***a* (cgs)**	***b***
BF95	2.94E-03	1.90
H04syn	6.10E-03	2.05
H04cnv	11.1E-03	2.40
H10all	5.28E-03	2.01
SZ10ave	4.34E-03	1.92

TABLE II – Merit factor of the comparison between $\mathrm{IWC}(\mathrm{PSD}, \mathbf{p}_{LI})$ *computed using the* $\mathbf{p}_{LI}$ *relations with the corresponding EIWC measurements.*

$\mathbf{p}_{LI}$	***NSE***	***NB***	$\boldsymbol{\rho}$
BF95	1.363	-0.872	0.8674
H04syn	2.637	-1.888	0.8677
H04cnv	2.768	-1.906	0.7582
H10all	1.854	-1.293	0.8546
SZ10ave	2.332	-1.620	0.8793

TABLE III – Coefficients a and b of the m-D relation (13) as a function of the different CWC class intervals $\hat{\mathbf{p}}_{pp}^{ci}$.

$\hat{\mathbf{p}}_{pp}^{ci}$	***a* (cgs)**	***b***
i	1.24E-03	1.693
ii	1.29E-03	1.736
iii	1.36E-03	1.816
iv	1.59E-03	1.977
v	1.95E-03	2.167
vi	2.59E-03	2.650

TABLE IV – Parameters of $\mathrm{IWC}(\mathrm{SRM}, \hat{\mathbf{p}}_{rm})$ *algorithms obtained using a nonlinear regression by minimizing the differences between the measured EIWC and its estimates obtained using (17) an (18).* $\mathrm{IWC}(\mathrm{PSD}, \hat{\mathbf{p}}_{rm})$ *is the optimized vector of coefficients for the different algorithms.*

$\hat{\mathbf{p}}_{rm}$	***α***	***β***	***γ***	***Δ***
ue	7.77E-02	0.208	-	-
ae	2.25E-02	0.526	-	-
we	2.31E-02	0.825	-	-
aou	2.00E-02	0.648	1.184	-
woa	3.88E-02	0.666	1.011	-
wou	1.81E-02	0.849	0.768	-
2dfr	2.60E-02	0.775	0.374	0.937

TABLE V – Merit factors of the comparison between IWC(PSD, $\hat{\mathbf{p}}_{rm}$) *estimates and the corresponding EIWC measurements computed using all the parameterizations of Table IV.*

$\hat{\mathbf{p}}_{rm}$	***NSE***	***NB***	$\boldsymbol{\rho}$
ue	0.769	-0.004	0.3891
ae	0.701	0.023	0.5453
we	0.441	0.024	0.8498
aou	0.664	0.021	0.6083
woa	0.431	0.002	0.8562
wou	0.432	0.021	0.8568
2dfr	0.407	0.012	0.8735

TABLE VI - Parameters of $\mathrm{IWC}(\mathrm{CRM}\hat{\mathbf{p}}_{dfr})$ *algorithms obtained using a nonlinear regression analysis by minimizing the differences between the measured EIWC and its estimates obtained from collocated radar measurements.*

$\hat{\mathbf{p}}_{dfr}$	α	β	γ	δ
ue	1.25E-01	0.112	-	-
ae	8.93E-02	0.213	-	-
we	1.09E-01	0.284	-	-
aou	7.74E-02	0.275	0.489	-
woa	9.74E-02	0.156	0.017	-
wou	9.00E-02	0.299	0.251	-
2dfr	7.75E-02	0.303	0.499	0.075

TABLE VII - Parameters of $\mathrm{IWC}(\mathrm{CRM}^{\mathrm{wet}}, \hat{\mathbf{p}}_{\mathrm{dfr}}^{\mathrm{wet}})$ *algorithms obtained using a nonlinear regression analysis by minimizing the differences between the measured EIWC and its estimates obtained from collocated radar measurements belonging to the wet slope class interval.*

$\hat{\mathbf{p}}_{\mathrm{dfr}}^{\mathrm{wet}}$	$\boldsymbol{\alpha}$	$\boldsymbol{\beta}$	$\boldsymbol{\gamma}$	$\boldsymbol{\delta}$
ue	8.46E-02	0.233	-	-
ae	7.14E-02	0.292	-	-
we	1.16E-01	0.318	-	-
aou	6.52E-02	0.322	0.681	-
woa	6.98E-02	0.347	0.245	-
wou	6.63E-02	0.368	0.224	-
2dfr	6.40E-02	0.371	0.481	0.157

TABLE VIII – Parameters of $\mathrm{IWC}(\mathrm{CRM}^{\mathrm{moist}}, \hat{\mathbf{p}}_{\mathrm{dfr}}^{\mathrm{moist}})$ *algorithms obtained using a nonlinear regression analysis by minimizing the differences between the measured EIWC and its estimates obtained from collocated radar measurements belonging to the moist slope class interval.*

$\hat{\mathbf{p}}_{\mathrm{dfr}}^{\mathrm{moist}}$	***A***	***β***	***γ***	***δ***
ue	1.01E-01	0.144	-	-
ae	9.96E-02	0.179	-	-
we	1.12E-02	0.251	-	-
aou	8.37E-02	0.244	0.339	-
woa	8.49E-02	0.227	0.101	-
wou	8.45E-02	0.233	0.081	-
2dfr	8.27E-02	0.238	0.941	-0.270

TABLE IX – *Parameters of* $\mathrm{IWC}(\mathrm{CRM}^{\mathrm{dry}}, \hat{\mathbf{p}}_{\mathrm{dfr}}^{\mathrm{dry}})$ *algorithms obtained using a nonlinear regression analysis by minimizing the differences between the measured EIWC and its estimates obtained from collocated radar measurements belonging to the dry slope class interval.*

$\hat{\mathbf{p}}_{\mathrm{dfr}}^{\mathrm{dry}}$	***A***	***β***	***γ***	***δ***
ue	1.06E-01	0.089	-	-
ae	9.75E-02	0.143	-	-
we	9.92E-02	0.230	-	-
aou	8.67E-02	0.230	0.371	-
woa	8.08E-02	0.133	-0.057	-
wou	8.17E-02	0.255	0.192	-
2dfr	8.78E-02	0.207	0.382	-0.075

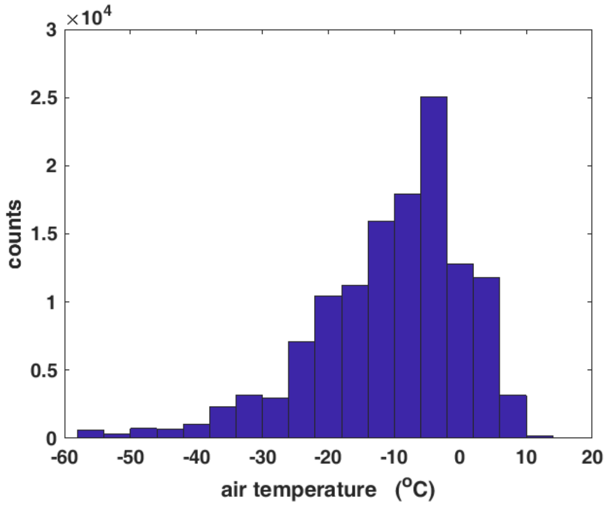

Figure 1 - Distribution of the air temperature recorded by the Citation aircraft during the observing periods of the OLYMPEX field experiment.

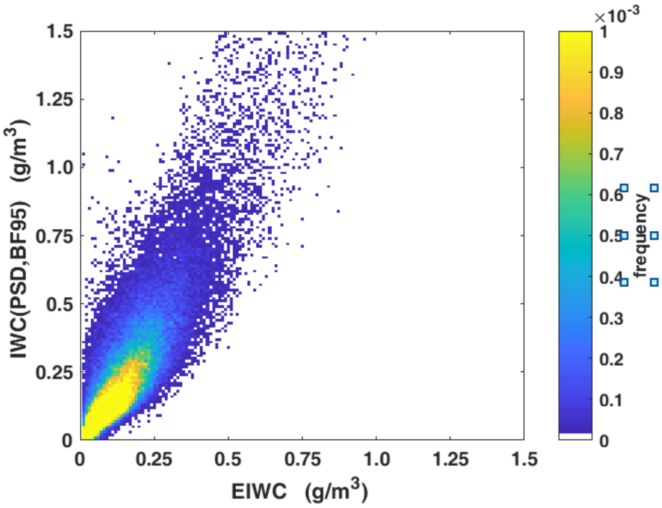

Figure 2 - 2-D histogram between the direct EIWC measurements versus the corresponding IWC(PSD,BF95) for the entire OLYMPEX dataset.

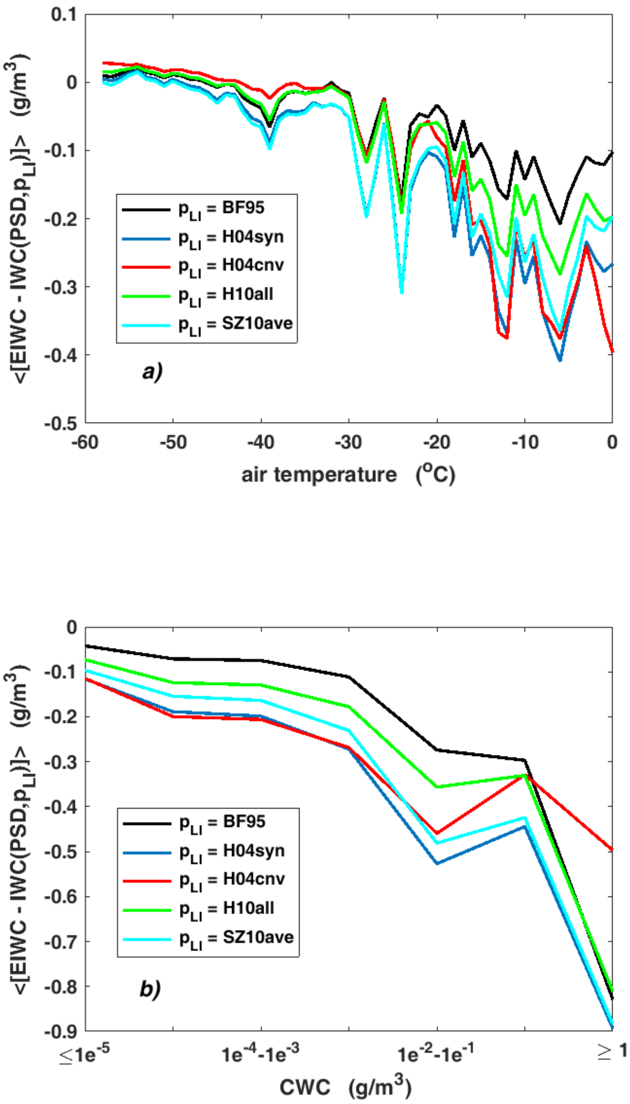

Figure 3 - Mean differences between EIWC measurements and IWC(PSD, $\mathbf{p}_{LI}$) *as a function a) of air temperature, and b) of cloud water content class intervals.*

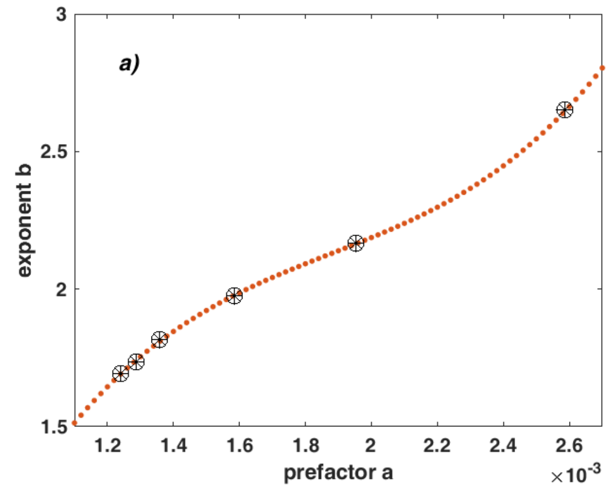

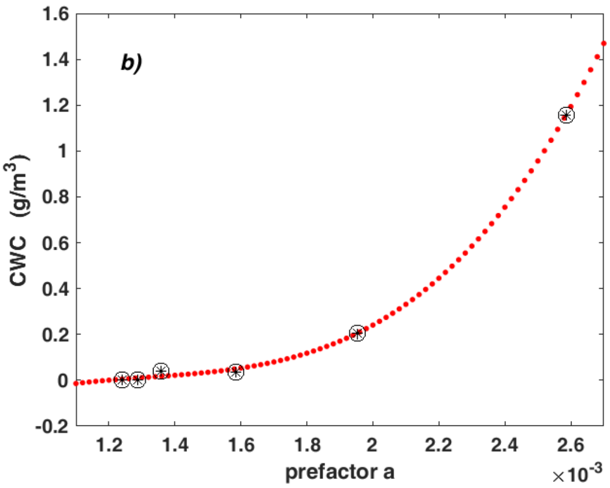

Figure 4 – a) the exponent b versus the prefactor a (black star-ring) regarding the m-D relationship for fixed CWC class intervals with the interpolation (dot red) line represented by a third-degree polynomial function, and b) the same CWC values versus the prefactor a (black star-ring) with the interpolation (dot red) line achieved by a third-degree polynomial function

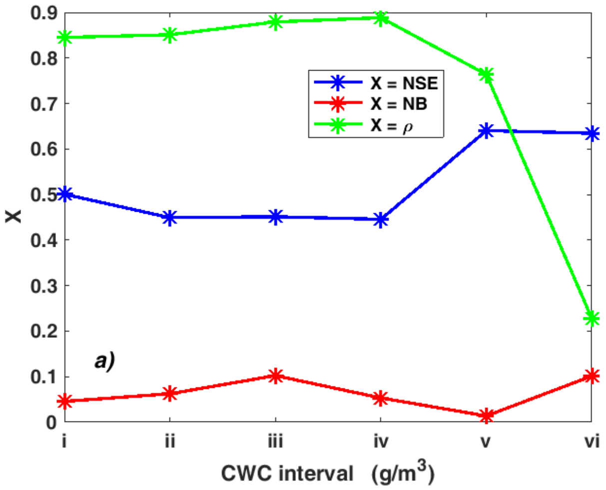

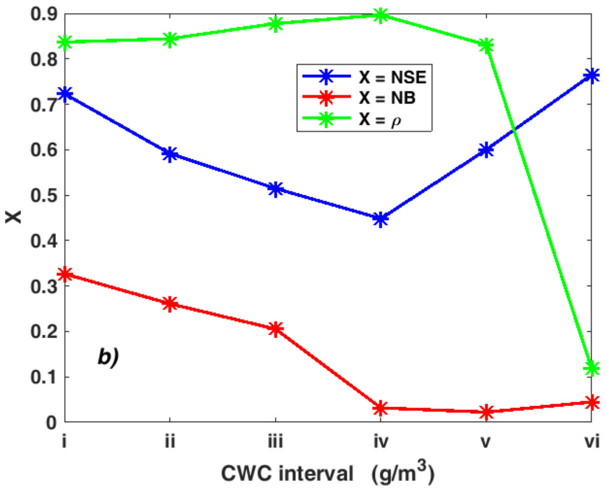

Figure 5 – NSE (blue), NB (red), and ρ (green) of: a) $\mathrm{IWC}(\mathrm{PSD}^{ci}, \hat{\mathbf{p}}_{pp}^{ci})$ *for the specific* $\hat{\mathbf{p}}_{pp}^{ci}$ *parameterizations, and b)* $\mathrm{IWC}(\mathrm{PSD}, \hat{\mathbf{p}}_{pp})$ *versus the corresponding CWC class intervals.*

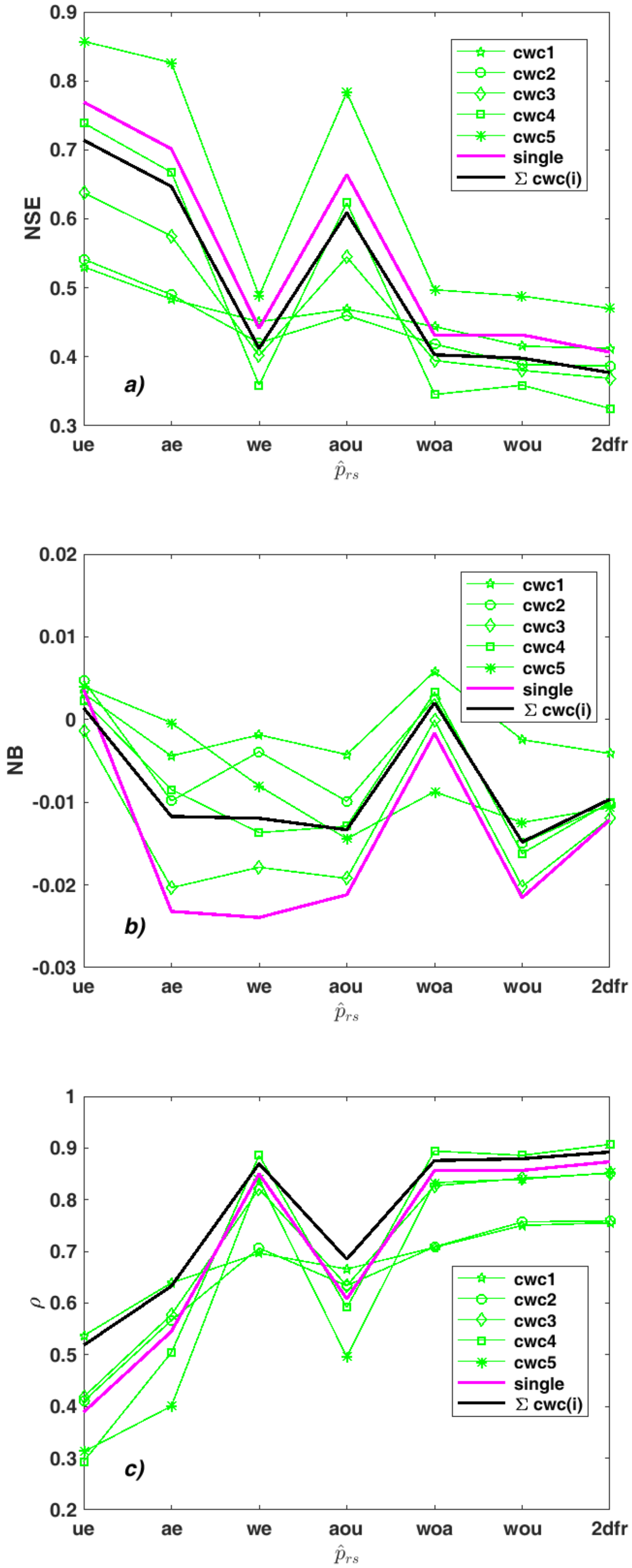

Figure 6 - a) NSE, b) NB, and c) ρ of the comparison between $\mathrm{IWC}(\mathrm{SRM}^{ci}, \hat{\mathbf{p}}_{rm}^{ci})$ *(green lines),* $\mathrm{IWC}(\mathrm{SRM}, \hat{\mathbf{p}}_{rm})$ *(magenta line),* $\mathrm{IWC}(\mathrm{SRM}^{ci}, \hat{\mathbf{p}}_{rm}^{ci})$ *composition (black line) obtained from the simulated reflectivities and EIWC for all the IWC radar algorithms.*

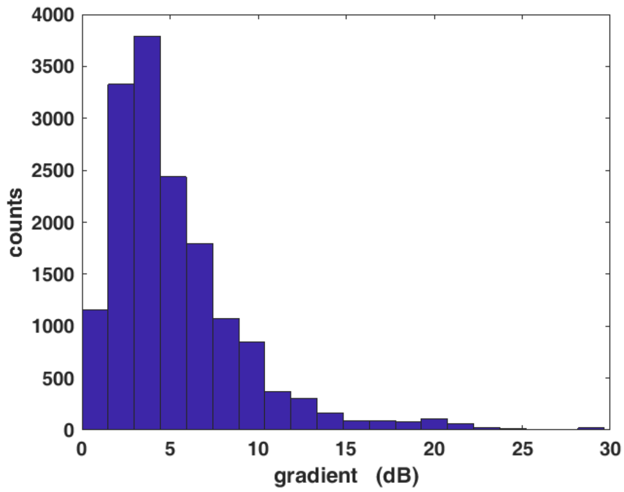

Figure 7 - Distribution of gradients contained in the space domain (2x2) km x 300 s. Gradients are represented by the difference between the maximum and the minimum Ku reflectivity contained in the domain.

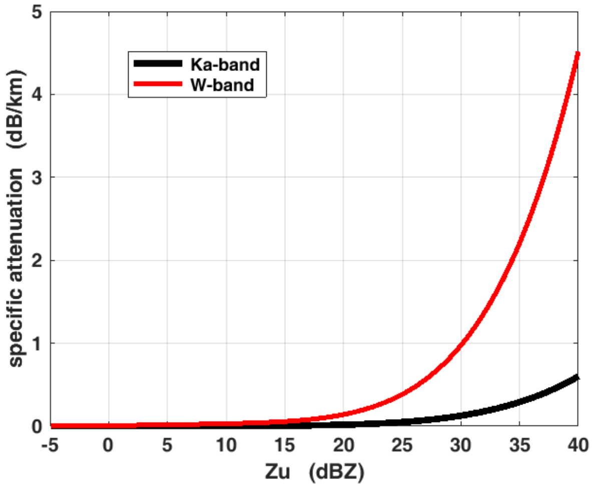

Figure 8 - Mean specific attenuations for the Ka- and W-band as a function of simulated Zu reflectivity.

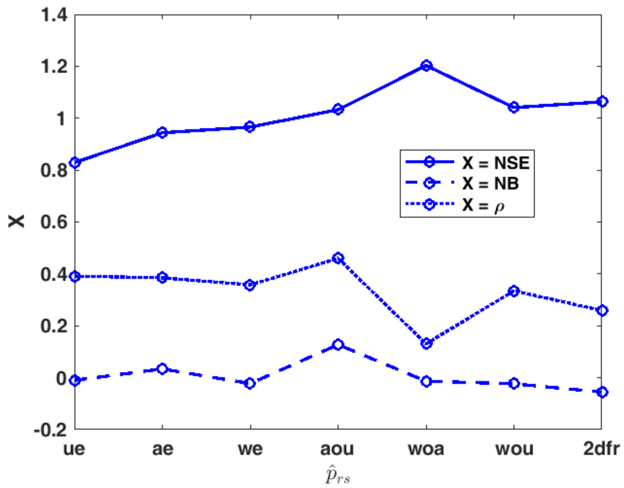

Figure 9 – Behavior of the merit factors NSE (solid line), NB (dash line), and ρ (dot line) of the comparison between $\mathrm{IWC}(\mathrm{SRM}, \hat{\mathbf{p}}_{rm})$ *estimates for all the* $\hat{\mathbf{p}}_{rm}$ *of Table IV applied to the collected radar measurements with the corresponding EIWC.*

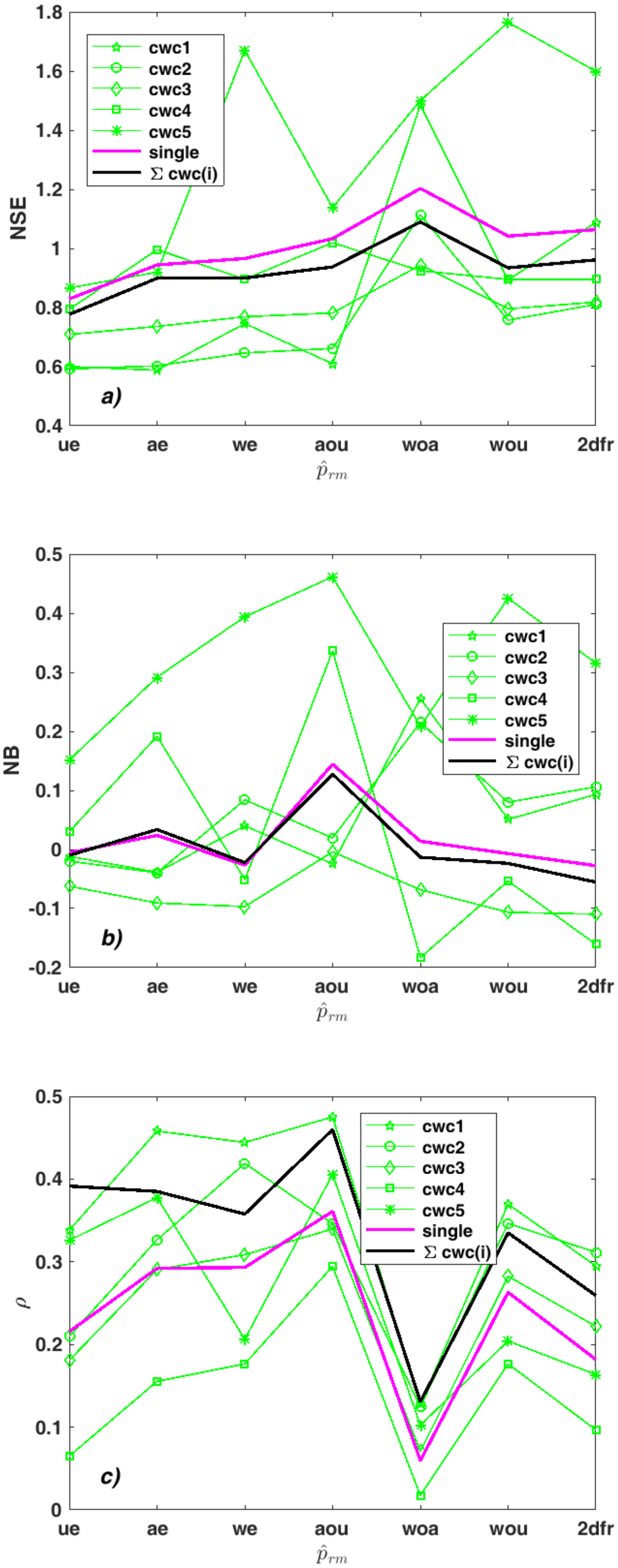

Figure 10 - *a) NSE, b) NB, and c) ρ of the comparison between* $\mathrm{IWC}(\mathrm{SRM}^{ci}, \hat{\mathbf{p}}_{rm}^{ci})$ *(green line),* $\mathrm{IWC}(\mathrm{SRM}, \hat{\mathbf{p}}_{rm})$ *(black line),* $\mathrm{IWC}(\mathrm{SRM}^{ci}, \hat{\mathbf{p}}_{rm}^{ci})$ *composition (magenta line) estimates obtained from the collocated radar measurements and EIWC for the considered IWC radar algorithms.*

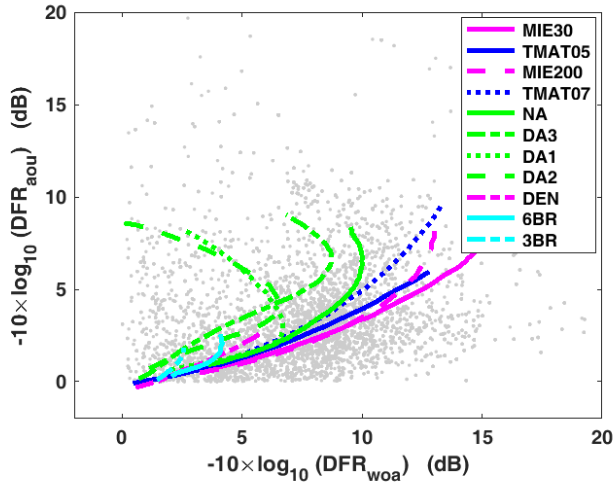

Figure 11 – Scatterplot of the dual frequency ratios DFR_{woa} and DFR_{aou} obtained from reflectivity measurements collected by the APR3. Overlaid for reference, displayed are some curves obtained by triple-frequency calculations for various ice particle scattering models by Kulie et al. (2014).

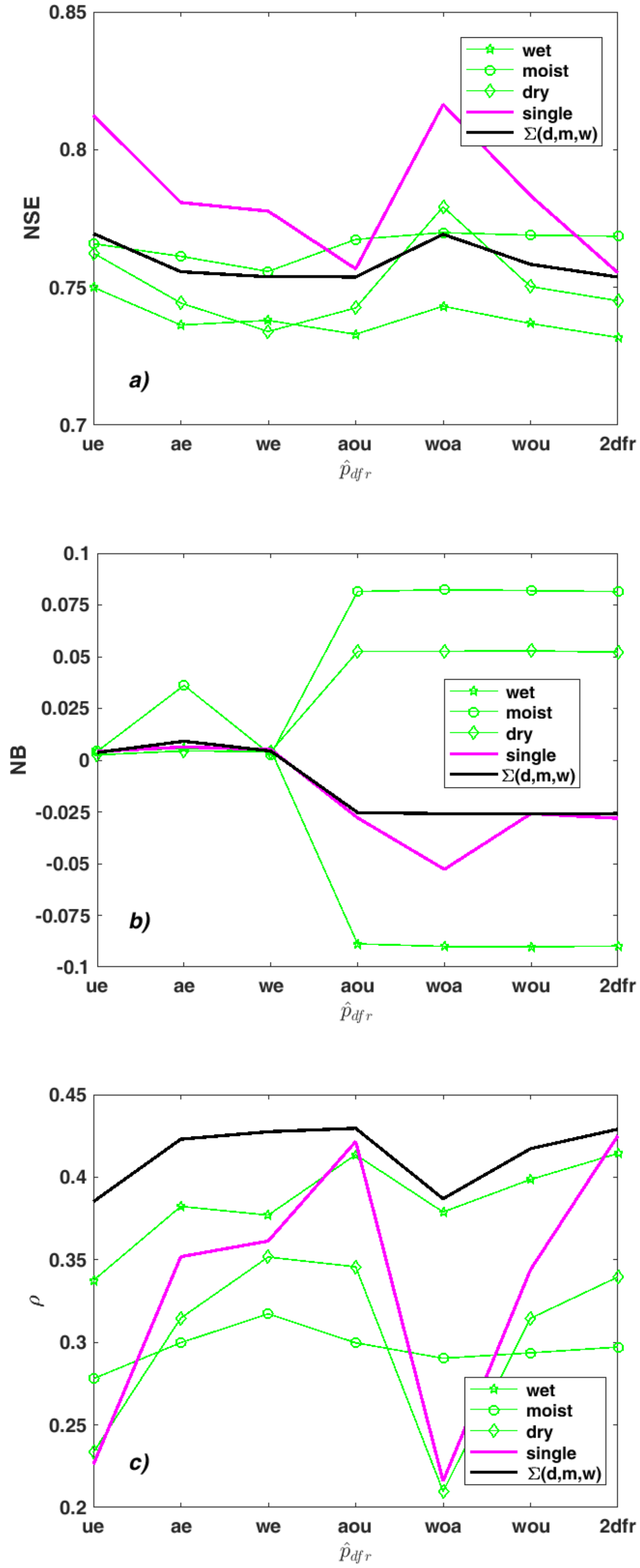

Figure 12 - a) NSE, b) NB, and c) ρ of the comparison between $\mathrm{IWC}(\mathrm{CRM}^{slp}, \hat{\mathbf{p}}_{dfr}^{slp})$ *(green line),* $\mathrm{IWC}(\mathrm{CRM}\hat{\mathbf{p}}_{dfr})$ *(black line),* $\mathrm{IWC}(\mathrm{CRM}^{slp}, \hat{\mathbf{p}}_{dfr}^{slp})$ *composition (magenta line) estimates obtained from reflectivity measurements collected by the APR3 and EIWC for all the considered IWC radar algorithms.*